

Title	Study on the Influence of Carbon Dioxide on the Oxy-Hydrogen Cutting Performance
Author(s)	Pinzón Acosta, César De Jesús
Citation	大阪大学, 2019, 博士論文
Version Type	VoR
URL	https://doi.org/10.18910/73577
rights	
Note	

Osaka University Knowledge Archive : OUKA

<https://ir.library.osaka-u.ac.jp/>

Osaka University

Doctoral Dissertation

Study on the Influence of Carbon Dioxide on the Oxy-Hydrogen Cutting
Performance

(二酸化炭素が水素ガス切断性能に及ぼす影響に関する研究)

By

César De Jesús Pinzón Acosta

July 2019

Division of Global Architecture
Graduate School of Engineering
Osaka University

Doctoral Dissertation (博士学位論)

Study on the Influence of Carbon Dioxide on the Oxy-Hydrogen Cutting
Performance

(二酸化炭素が水素ガス切断性能に及ぼす影響に関する研究)

By

César De Jesús Pinzón Acosta

Department of Naval Architecture and Ocean Engineering

Division of Global Architecture

Graduate School of Engineering

Osaka University

2019

Supervisor (指導教官): Professor Naoki Osawa

Dissertation Committee:

Professor Masahiko Fujikubo

Professor Ninshu Ma

Professor Naoki Osawa

Associate Professor Seiichiro Tsutsumi

Abstract

During the last years, there has been a growing interest on using Hydrogen (H_2) for the preheating flame of the oxy-fuel cutting since the use of H_2 improves the cutting performance, reduces the thermal distortion of the workpiece as well as the Carbon Dioxide (CO_2) emissions during the process. In practical applications of oxy-hydrogen cutting, fossil gas is mixed with H_2 to improve the preheating flame visibility and process safety. The addition of fossil gases deteriorates the cutting performance, but the mechanism of this deterioration has not been clarified yet. There is a significant incentive to clarify the mechanism of the process and optimize the preheating gas composition, and these are objectives of this study.

The present study is composed of six chapters, as follows:

Chapter 1 gives a background of this study. Current problems and challenges concerning Oxy-Hydrogen cutting are presented. Additionally, this chapter states the problem, objectives and the structure of this study.

Chapter 2 presents the numerical theory used in this study. An inverse heat conduction analysis (IHCA) method which can identify the local heat transfer parameters (the gas temperature right on the plate surface, T_G , and the heat transfer coefficient, α) of the preheating flame, is proposed. A quasi-static three-dimensional finite element code that employs a moving coordinate system is developed. This

code can perform heat conduction analysis in which the heat supply due to preheating q_G and that due to metallic combustion q_B are separately assessed. A new estimation technique of the kerf temperature distribution based on the two-dimensional Matsuyama's solution is developed.

Chapter 3 presents the description and results of the experimental tests. Spot heating tests of thin circular plate are performed to identify T_G and α of H_2 , H_2 - CO_2 mixed and H_2 -AR mixed gasses by using the IHCA method developed in Chapter 2. Piercing tests of thick steel plate, in which the minimum piercing time, t_{min} , is measured, are performed to validate T_G and α identified by the IHCA method. Cutting tests of thick steel plate are performed, and the groove geometry (cutting front shape, curvature of the cutting front, kerf width) are measured for various preheating gas conditions.

Chapter 4 presents the numerical results of IHCA for the spot heating test results and the direct thermal conduction analysis (DHCA) of the piercing tests. T_G and α are identified from thin plate's temperatures measured in the spot heating tests. Thick plate's heating face temperatures in the piercing tests are analyzed by DHCA where the heat transfer parameters T_G and α are adopted. By employing the steel kindling temperature as the prerequisite for the piercing process, t_{min} is calculated. The results from the numerical simulation and the measured t_{min} show good agreement.

The obtained results show the validity of the identified local heat transfer parameters and the developed IHCA method. It is found that the heat efficiency and piercing performance of the Hydrogen preheating flame deteriorates with the increase of the inert gas's mixing ratio, and the use of CO₂ has a harmful effect on the cutting performance.

Chapter 5 presents the numerical results of three-dimensional quasi-static FE analyses of the oxy-hydrogen cutting process. It is shown that the kerf temperature estimation technique developed in Chapter 2 can achieve a smooth three-dimensional kerf temperature distribution for cases with heavy thickness and inclined cutting fronts. It is also shown that q_G shows substantial decline while q_B remains unchanged when CO₂ is added to H₂ gas. This suggests that the cutting performance deterioration due to CO₂, reported in the literature, is caused solely by the decrease in the heat transfer from the preheating flame.

Chapter 6 summarizes the conclusion and the contributions of this study. Additionally, recommendations for further works than can be implemented in this analysis and may improve the validity of the proposed technique are presented.

Table of Contents

Abstract	iii
Table of Contents	vii
Chapter 1: Introduction	1
1.1 Overview	1
1.2 Oxy-fuel Cutting	2
1.2.1 Process description	2
1.2.2 Oxy-hydrogen cutting	5
1.3 Literature Review	7
1.4 Problem Statement	11
1.5 Objectives and Structure	12
Chapter 2: Methods of Analysis	15
2.1 Introduction	15
2.2 Numerical Estimation of Heat Transfer Parameters	15
2.2.1 Heat transfer parameters between gas flame and steel plate	15
2.2.2 Genetic representation of heat transfer parameters	17
2.2.3 Fitness function	20

2.3	Three-dimensional Gas Cutting Simulation	21
2.3.1	Kerf temperature.....	21
2.3.2	Heat conduction analysis using a moving coordinate system.....	23
2.3.3	Translation of the temperature field	25
2.3.4	Two-dimensional surface temperature field.....	26
2.3.5	Three-dimensional temperature field	26
2.3.6	Three-dimensional temperature field adjustment.....	28
2.4	Conclusions.....	30
Chapter 3: Experimental Tests.....		31
3.1	Introduction.....	31
3.2	Spot Heating Test	32
3.2.1	Experimental setup	32
3.2.2	Results	35
3.2.3	Discussion.....	36
3.3	Piercing Tests.....	37
3.3.1	Experimental setup	37
3.3.2	Results	39

3.3.3 Discussion.....	40
3.4 Gas Cutting Tests.....	40
3.4.1 Experimental setup.....	40
3.4.2 Measurement results.....	42
3.4.3 Discussion.....	43
3.5 Conclusions.....	46
Chapter 4: Numerical Simulation of the Piercing Process	48
4.1 Introduction.....	48
4.2 Identification of Heat Transfer Parameters	49
4.2.1 Model description.....	49
4.2.2 Estimation of heat transfer parameters.....	51
4.3 Heat Flux Distribution Estimation.....	59
4.4 Estimation of Piercing Performances	62
4.4.1 Model description.....	62
4.4.2 Piercing time estimation.....	63
4.5 Conclusions.....	66
Chapter 5: Numerical Simulation of the Gas Cutting Process	68

5.1	Introduction.....	68
5.2	Gas Cutting Simulation	69
5.2.1	Implementation of moving coordinate analysis	69
5.2.2	Model description.....	69
5.2.3	Kerf temperature estimation.....	75
5.3	Cutting Performance Analysis.....	87
5.4	Conclusions.....	90
	Chapter 6: Conclusion and Recommendations.....	92
6.1	Introduction.....	92
6.2	Conclusions and Contributions.....	92
6.3	Recommendations	96
	References.....	98
	List of Publications	105
	Acknowledgements.....	106

Chapter 1

Introduction

1.1 Overview

During metal structure fabrication, very rarely does steel come in the shape or size needed. Thermal cutting is an essential step in the production of steel structures worldwide. Major thermal cutting processes include oxy-fuel, plasma, and laser cutting. The thermal cutting method best suited for the job is usually chosen based on the workpiece requirements.

In case of thick plate processing, oxy-fuel cutting process stands out, among other thermal cutting methods because of its relatively easy setup configuration and the operational costs. The oxy-fuel cutting process allows the processing of thick plates, limited only by the amount of oxygen that can be delivered during the process. In this regard, the torch flame conditions employed during the process have a significant impact on cut quality. When the torch flame conditions are appropriately adjusted,

the oxy-fuel cutting process delivers a smooth, square cut surface, and the obtained cutting quality is suited for many applications without any further treatment.

1.2 Oxy-fuel Cutting

1.2.1 Process description

The oxy-fuel gas cutting also known as burning or flame cutting, includes a group of thermal processes that employs a controlled chemical reaction to remove the preheated metal by rapid oxidation of the material by a stream of pure oxygen [1]. During the oxy-fuel cutting process, a workpiece is heated by a preheating flame until it reaches its kindling temperature (the temperature at which steel rapidly oxidized) [2], then a stream of oxygen is blown into the workpiece which triggers an exothermic reaction of the steel that generates additional heat that cut the material. As the cut progresses, the metal in the path of the oxygen stream burns to make a narrow slot usually referred to as kerf. During the process, the operator manually adjusts the pressure of both the oxygen and the preheating flame to control the flame temperature.

For a successful cutting [3], the material to be cut must fulfill certain conditions:

- The oxide must have a melting point that is lower than the melting point of the metal itself. It is the melting temperature of the oxides that explains why stainless steel and aluminum are not suitable for oxy-fuel cutting.
- The ignition temperature of the metal must be lower than its melting point.
- Combustion of the metal must create sufficient heat to maintain combustion.

The cutting torch is moved at a speed that maintains an acceptable cut quality. Major factor affecting the cut quality includes, the oxygen pressure, the preheating flame pressure, the standoff distance, and the nozzle specifications. The cut quality ultimately depends on the skill of the operator who controls all these variables for an specific material with a given thickness [4].

The preheating flames initiates the exothermic reaction and sustain the reaction by continuously heating the metal at the line of the cut. Additionally, the flame removes any scale or dirt that may interfere with the cutting process [5]. The rate of heat transfer in the workpiece influences the heat balance for cutting. As the thickness of the material to be cut increases, more heat is needed to keep the metal at its ignition temperature. Generally, Acetylene (C_2H_2) [6] is used with oxygen to provide the preheat flame but other gases can be used such as Propane (LPG) or Hydrogen (H_2) [7] [8].

If oxygen flow is insufficient, or the cutting speed is too high, the lower portions of the cut react more slowly, and the cutting face curves behind the torch. The horizontal distance between point of entry and exit is called drag as shown on Fig. 1.1.

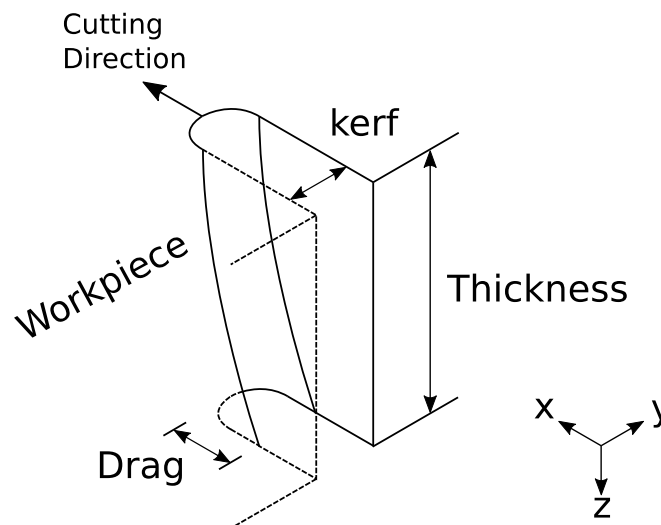


Fig. 1.1 Schematic view of the workpiece after the oxy-fuel cutting process.

The drag directly influences the cut edge quality. Optimum edge quality results from zero drag. It is usually achieved when the oxygen stream enters and leave the cut in a straight line along the cutting tip axis. Increasing the cutting speed or reducing oxygen flow makes less oxygen available at the bottom of the cut, causing the bottom of the cut to drag behind the top of the cut. Quality cuts are often achieved by controlling the heat input of the process. Higher quality demands less drag: more

drag indicates poorer quality and low oxygen consumption. Excessive drag may lead to incomplete cutting. In very thin sections, drag has little significance. However in thick sections, the goal is to avoid excessive drag [9].

1.2.2 Oxy-hydrogen cutting

H₂ is a colorless and odorless elementary gas. In nature it is rarely found in its atomic form. It is a highly flammable gas that when mixed with air, forms an explosive mixture. The chemical reaction of complete combustion of H₂ and Oxygen (O₂) only produces water H₂O [10]. In terms of flame combustion, one of the key differences between Hydrogen combustion and Hydrocarbons combustion is the production of carbon dioxide (CO₂) [11]. Some of the properties that make H₂ attractive for the oxy-fuel cutting process are its high thermal conductivity and diffusivity. It is the lightest gas, also has a minimum energy requirement for ignition, and has a high rate of combustion.

Table 1.1 Cutting gas reaction formula

Gas	Reaction Formula
Hydrogen	$2 \text{H}_2 + \text{O}_2 \rightarrow 2 \text{H}_2\text{O}$
Acetylene	$2 \text{C}_2\text{H}_2 + 5 \text{O}_2 \rightarrow 4 \text{CO}_2 + 2 \text{H}_2\text{O}$
Propane	$\text{C}_3\text{H}_8 + 5 \text{O}_2 \rightarrow 3 \text{CO}_2 + 4 \text{H}_2\text{O}$

During the last years, as the demand of extra thick plate processing has increase worldwide, there has been a growing interest in using H₂ for the preheating flame of the oxy-fuel cutting process due to its properties since the use of H₂ improves the cutting performance [10] [12], reduced the thermal distortion of the workpiece, and also reduce CO₂ emissions during the process. In practical application of oxy-hydrogen cutting, the preheating flame is composed of a mixture of gases. Generally, H₂ is mixed with a fossil gas, such as LPG, to improve the visibility of the preheating flame since the H₂ flame is almost invisible and the flame condition hard to adjust. Additionally, by using a fossil gas helps to avoid drastic explosions during the mixture gas ignition, improving the process safety [11]. However, one of the side effects of mixing fossil gases in the preheating flame is the reduction of cutting performance. In this regard, the precise deterioration mechanism of the process has not been fully clarified yet. Another significant concern with the oxy-hydrogen preheating flame is that the flame optimization process is performed manually and usually relies on the individual skill of experienced workers. As a result, there is a considerable incentive to automate the preheating flame adjustment along with the gas composition optimization as much as possible. The automation of the oxy-hydrogen cutting process in terms of the preheating flame adjustment and the gas composition optimization is highly desirable for the shipbuilding industry in term of quality, efficiency and production rates. However, in order to automate the process,

clarification on the relationship between the preheating flame conditions and the cutting performance needs to be addressed.

1.3 Literature Review

The oxy-fuel cutting is a very complex process. It affects the material microstructure, its hardness and mechanical properties. Additionally, the process introduces surface roughness and residual stresses to the workpiece [13]. Next, a literature review of the research works devoted to studying the oxy-fuel cutting process is detailed.

Direct measurement and observation of the oxy-fuel cutting process are often difficult because of the severe operating conditions. Moreover, the process is influenced by many factors [14] (e.g., the plate thickness, the preheating state, simultaneous solid/liquid/gas interactions, chemical reactions, heat and mass transfer), that are difficult to implement on analytical models. In this regards the first mathematical formulation for the heat conduction from a line source in an infinite solid had been proposed by Rosenthal [15] for materials with thermal properties invariant with temperature.

Initial investigations of the process focused on the assessments of cut width, cutting speed, nozzle diameters, oxygen pressure, and flow rate and fuel-gas flow

rate for various steel plate thicknesses. For example, Suitsu [16] [17] focused on the role of the preheating flame in the oxy-fuel cutting process. Nakanishi [18] [19] [20] [21] studied the shielding effect of oxygen, the surface activation effect, and the maximum cutting thickness during the oxy-fuel cutting process. Ueda [22] study the effect of the preheating flame pressure in the oxy-fuel cutting process. These investigations helped considerably in the selection of optimum conditions for making straight cuts on plates. However, these studies could not derive the relationship of the preheating flame conditions (e.g., the gas composition, the fossil gas) and the cutting performances (e.g., the cutting speed, the thermal distortion).

Further investigations on the oxy-fuel cutting process comes from the analysis of the oxidation reaction. In this regard, most of the studies have been focused on laser-oxygen cutting which in principle is similar to the oxy-fuel cutting process. Sato et al. [23] studied the ignition process of iron in an oxygen atmosphere, Ivarson et al. [24] studied the effects of oxygen purity during laser cutting of mild steel. Powell et al. [25] proposed a series of guidelines to be considered during the modeling of laser-oxygen cutting of mild steel. El-Rabii et al. [26] proposed an analytical model of the dynamic combustion. These investigations are of great value to understand the mechanism of the mild steel combustion in oxygen flows. However due to the number of parameters considered in these analyses it is very difficult to implement the mathematical models in the oxy-fuel cutting process.

To assess the heat input required to produce a cut of given width and speed, a quantitative study of heat flow by metallic conduction must be addressed [27]. In the regard, Wells [28], for the first time established a relationship between significant variation of shape of weld ripples and heat input rates during the welding process. Terasaki et al. [29] experimentally investigated the heat input generated during the gas cutting process. In the analysis the identified thermal flux distribution was approximated by considering a Gaussian distribution of the heat input. However, the preheating heat input was evaluated without the contributions made by the gas thermal flux within the cutting groove.

Osawa et al. [12] developed a method to study the thermal effects of the preheating flames during the piercing process. In this study, the distribution of the heat transfer parameters, the gas temperature T_g and the local heat transfer coefficient α were identified by performing an inverse heat conduction analysis of a thin circular plate during spot heating test. This method was applied to analyze the piercing performance of an oxy-hydrogen preheating flame (H_2 -LP), and an oxy-fuel preheating flame (LPG). They reported the superiority of the oxy-hydrogen preheating flame in terms of the local heat transfer efficiency.

Osawa et al. [30] developed a finite element code to perform a three-dimensional heat conduction analysis in which the preheating and the material combustion heat input are separately assessed. Their method was used to analyze gas cutting tests

using the preheating flames H₂-LP, and LPG. Although they successfully show the ratio of the preheating heat input and the material combustion heat input for the selected gases, the preheating flame composition effect was not taken into consideration as they used a fixed mixing ratio of H₂-LP and 100%LPG. On the other hand, the analysis is focused on thin plates (12 mm) where the cutting front inclination can be neglected.

Ikegami [31], studied the influence of CO₂ on the cutting performance by performing gas cutting tests of 50 mm thick plates using H₂ and a mixture of H₂-CO₂ gases. As a result, he reported that the cutting performance declined with the increase of CO₂ mixing ratio, and that CO₂ affects the metallic combustion during the process. However, from this study it is not clear the reason of the deterioration whether it is originated by the preheating flame heat input or by the metallic combustion heat input.

The numerical simulation of the oxy-fuel cutting process considering the heat input from the preheating flame and the material combustion have been successfully established by several authors [32] [33] [34]. However, these studies considered idealized heat sources models that cannot take into consideration the characteristics of the preheating flame state. In the regard, the method developed by Osawa et al. [30] allows the evaluation of the practical conditions of the oxy-fuel cutting process.

1.4 Problem Statement

Although the oxy-fuel cutting process has improved over time, it strongly relies on the knowledge and skill of the operator. Unfortunately, the inheritance of this skills is a very difficult task that takes long time and cost to master, and it may reduce the productivity of the shipyards if it is not carefully planned. The advantages associated with the oxy-hydrogen cutting automation in terms of preheating flame adjustment, and gas composition optimization are of great value for shipyards concerning the quality, efficiency and production rate for thick plate processing.

In order to automate the preheating flame adjustment, clarification on the relationship of the preheating flame condition and the cutting performance needs to be addressed. Ikegami's [31] results shows the importance of the separate evaluation of the preheating heat input and the material combustion heat input, and also the need to consider the preheating flame composition during the analysis. Although Osawa et. al [30] successfully analyzed the ratio of the preheating heat input and the material combustion heat input of the oxy-fuel cutting process for thin plates, it is necessary to study this relationship for thicker plates (> 12 mm), where the oxy-fuel cutting process achieves its highest efficiency and produced the most satisfactory cuts.

By considering that CO₂ is a product of the preheating flame combustion, the present study is devoted to study the influence of the CO₂ on the oxy-hydrogen cutting performance in terms of the CO₂ content on the preheating flame, and the CO₂ heat transfer role on the cutting process. To study the influence of CO₂ content on the preheating flame a numerical simulation of the piercing process is carried out and validated with an experimental piercing process test. On the other hand, to study the heat transfer role of CO₂, a simulation of the oxy-hydrogen cutting process is performed. Based on these simulation results, CO₂'s deterioration mechanism on the cutting performance is compared with Ikegami's [31] gas cutting test results.

1.5 Objectives and Structure

The results of this study will help to clarify the relationship between the preheating flame state and the performance of the oxy-fuel cutting process. In this regard, it will help to solve the skill inheritance problem, providing an alternative for the preheating flame adjustment and allowing to find optimum preheating flame properties for the selected preheating gas. In the same manner, the study can contribute to the environmental protection by improving the oxy-hydrogen cutting performance and the promotion of hydrogen gas cutting among other gases.

The present work is divided into six chapters; below is detailed the structure of this study:

Chapter 1 presents the background of the oxy-fuel gas cutting, as well as the problems and challenges when analyzing the process. Additionally, the problem statement, the objectives, and the outlook of this study is presented.

Chapter 2 discusses the numerical theory used during this study. It revises the formulation for the estimation of the heat transfer parameters and the piercing times as well as the formulation for the three-dimensional heat conduction analysis of the oxy-hydrogen cutting process.

Chapter 3 presents the description and results of the experimental tests carried out during this study. Spot heating test is performed to identify the heat transfer parameters, piercing test are carried out to quantify the performance of the preheating flames and gas cutting test are performed to measure the cutting front geometry after the cutting process.

Chapter 4 presents the numerical simulation of the piercing performance. This chapter also review the identification of the heat transfer parameters as well as the validation.

Chapter 5 discusses the three-dimensional simulation of the oxy-hydrogen cutting process. The first half of the chapter present the methodology used during

the analysis. A new technique for the kerf temperature estimation considering inclined cutting fronts is established. The ratio of the preheating heat input and the material combustion heat input is examined. Based on the simulation results, CO₂ deterioration mechanism on the cutting performance is then discussed.

Chapter 6 summarizes the conclusions as well as the contributions in this study. Also, recommendations for further works than can be implemented in this analysis and may improve the validity of the proposed technique are presented.

Chapter 2

Methods of Analysis

2.1 Introduction

In order to understand the relationship between the preheating flame state and its influence on cutting performance, numerical simulations of the cutting process are prepared. Numerical simulations of both the piercing process and the gas cutting process are carried out to analyze the influence of CO₂ in the cutting performance. The theories behind these numerical simulations are detailed in the next sections.

2.2 Numerical Estimation of Heat Transfer Parameters

2.2.1 Heat transfer parameters between gas flame and steel plate.

Osawa et al. [35], proposed a hypothesis on heat transmission during line heating which assumes that the distribution of the temperature of the gas adjacent to the heated surface T_G , and the local heat transfer coefficient α are time independent,

therefore they only depend on the distance from the torch. This hypothesis is based on the measurement of gas temperature fields within the combustion flames during spot heating test, by using a laser induced fluorescence (LIF) measurement system [36]. This hypothesis can be represented in terms of a linear relationship between the heat flux q and the heated surface temperature T_S as shown in Eq. 2.1.

$$q(t; r) = -\alpha(r)T_S(t; r) + \alpha(r)T_G(r) \quad (2.1)$$

Time histories of plate backface temperature T_B are recorded during a spot heating test, as shown in Fig. 2.1. Time histories of q and T_S can be estimated by an inverse heat conduction analysis from the recorded T_B . The gas temperature T_G and the heat transfer coefficient α can be identified by a linear regression analysis on the relation between q and T_S .

Osawa et al. [12], proposed a direct identification technique for T_G and α based on genetic algorithms. The validity of this technique was demonstrated by comparing the identified T_G and the one measured by LIF system. The results of this study [12], demonstrate that the proposed technique allows the evaluation of cases where ignition temperature on the workpiece surface is reached.

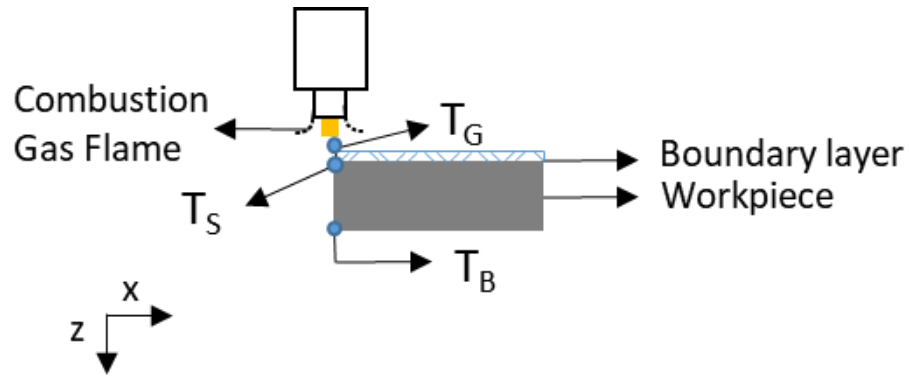


Fig. 2.1 Schematic view of the spot heating test.

2.2.2 Genetic representation of heat transfer parameters

Hereafter, r denotes the distance from the nozzle center, R_0 is the distance from the nozzle center to the spouts of preheating, and R_E is the outer end of the analysis region, as shown in Fig 2.2b. The region with $0 < r < R_0$ is called “inner region”, and that with $R_0 < r < R_E$ “outer region”

In Osawa’s analysis, the following considerations were taken in order to analyze the preheating for the oxy-fuel gas cutting:

- T_G shows its maximum at $r = R_0$, and the maximum T_G is close to the theoretical flame temperature.
- T_G approaches room temperature at $r = \infty$.
- α shows its maximum at $r = R_0$.
- α approaches the natural convection heat transfer coefficient when $r = \infty$.

Based on these assumptions, T_G and α are represented as follows:

a) Set the upper and lower bound of T_G and α at $r = 0$, r_0 , and r_E

$$T_{C,min}, T_{C,max}, T_{0,min}, T_{0,max}, T_{E,min}, T_{E,max}, \alpha_{C,min}, \alpha_{C,max}, \alpha_{0,min}, \\ \alpha_{0,max}, \alpha_{E,min}, \alpha_{E,max}.$$

b) Give T_G and α at $r = 0$, $r = r_0$, and $r = r_E$ as:

$$\begin{aligned} T_C &= T_{C,min} + d_C(T_{C,max} - T_{C,min}) \\ \alpha_C &= \alpha_{C,min} + e_C(\alpha_{C,max} - \alpha_{C,min}) \\ T_0 &= T_{0,min} + d_0(T_{0,max} - T_{0,min}) \\ \alpha_0 &= \alpha_{0,min} + e_0(\alpha_{0,max} - \alpha_{0,min}) \\ T_E &= T_{E,min} + d_E(T_{E,max} - T_{E,min}) \\ \alpha_E &= \alpha_{E,min} + e_E(\alpha_{E,max} - \alpha_{E,min}) \end{aligned} \quad (2.2)$$

Where $d_C, e_C, d_0, e_0, d_E, e_E$ are real numbers ranging from 0 to 1.

c) Arrange the number of control points n_i inside the inner region, and enumerate them ($i_I = 1, 2, \dots, n_i$) as the distance from the center of the nozzle ($r = r_0$) increases. Give T_G and α at each control point as:

$$\left. \begin{aligned} T_{I1} &= T_C = f_1(T_{max} - T_C), \alpha_{I1} = \alpha_C = g_1(\alpha_{max} - \alpha_C) \\ T_{I2} &= T_C = f_2(T_{I1} - T_C), \alpha_{I2} = \alpha_C = g_2(\alpha_{I1} - \alpha_C) \\ &\vdots \end{aligned} \right] \quad (2.3)$$

Where $f_1, g_1, f_2, g_2, \dots$ are real numbers ranging from 0 to 1.

- d) In the same manner as c, arrange the number of control points n_0 in the outer region, and enumerate them ($i_0 = 1, 2, \dots, n_0$) as the distance from the spout ($r = r_E$) increases. Give T_G and α at each control point as:

$$\left. \begin{aligned} T_{O1} = T_E = h_1(T_{max} - T_E), \alpha_{O1} = \alpha_E = k_1(\alpha_{max} - \alpha_E) \\ T_{O2} = T_E = h_2(T_{O1} - T_E), \alpha_{O2} = \alpha_E = k_2(\alpha_{O1} - \alpha_E) \\ \vdots \end{aligned} \right] \quad (2.4)$$

Where $h_1, k_1, h_2, k_2, \dots$ are real numbers ranging from 0 to 1.

- e) T_G and α between the control points are given by 3rd order spline interpolation. $2 \times 3 + 2 \times n_1 + 2 \times n_0$ number of real numbers $d_C, e_C, d_0, e_0, d_E, e_E, f_1, g_1, f_2, g_2, h_1, k_1, h_2, k_2$ are the genes of employed during the genetic algorithm analysis. An example of genetic representation of T_G and α is shown in Fig. 2.2

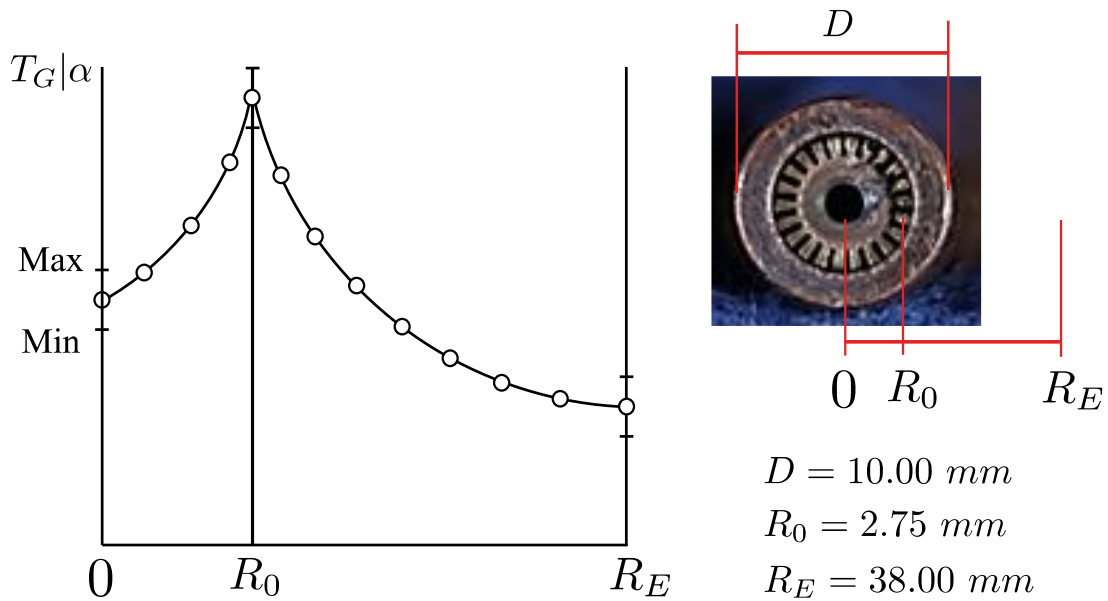


Fig. 2.2 Representation of the heat transfer parameters distribution over the region of analysis. (a) gas flame temperature and heat transfer coefficient distribution. (b) employed gas nozzle and the analysis region.

2.2.3 Fitness function

The distributions of T_G and α are identified by carrying out spot heating test of a thin circular plate. Let $B_{J,K}$ be the measured plate back face temperature at the J-th measurement point ($J=1,2,\dots,N_B$) at time t_k ($K=1,2,\dots,N_T$), and $Y_{J,K}$ be the calculated temperature at the same point and time. The fitness function E is defined as follows,

$$E = \frac{\sum_{K=1}^{N_T} \sum_{J=1}^{N_B} (Y_{J,K} - B_{J,K})^2}{\sum_{K=1}^{N_T} \sum_{J=1}^{N_B} (B_{J,K})^2} \quad (2.5)$$

2.3 Three-dimensional Gas Cutting Simulation

2.3.1 Kerf temperature

Matsuyama et al. [37] developed a technique in where the heat flux through the kerf is determined so that it is the same as the heat flux necessary for melting the metal to be cut at the cutting groove's leading edge. A quasi-stationary heat conduction field around the moving heat source is determined so that the temperature at the groove leading edge is kept at the melting point, and the adiabatic condition is fulfilled at the groove surface at the rear of the torch.

Matsuyama et al. [37] proposed to determine the coefficients of two-dimensional quasi-stationary heat conduction field around a moving heat source so that they minimize the residual error between the temperature/thermal flux and the thermal boundary conditions at multiple evaluation points on the cutting groove. The boundary conditions of the cutting groove used in Matsuyama et al.'s [37] analysis are shown in Fig. 2.3. At the leading edge (the S_1 boundary in Fig. 2.3), the temperature equals the melting point of the material. The kerf is assumed to be adiabatic and well separated from the torch to the rear (the S_3 boundary in Fig. 2.3).

The temperature and flux between S_1 and S_3 (the S_2 boundary in Fig. 2.3) are calculated by using the determined coefficients.

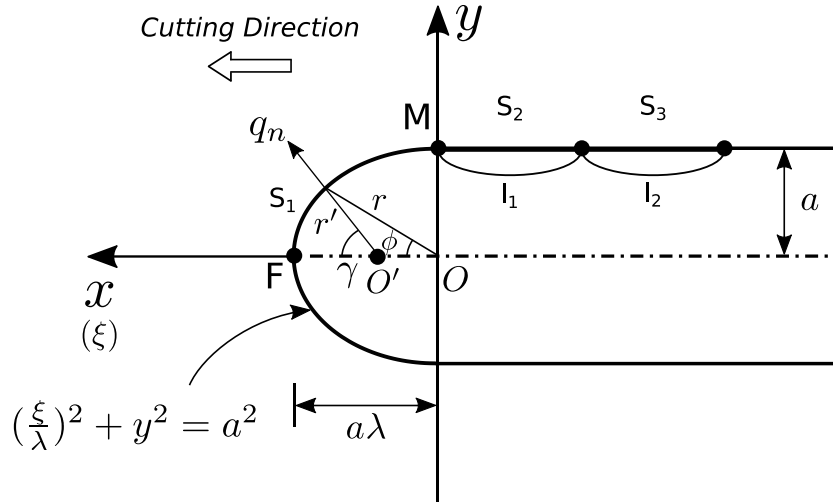


Fig. 2.3 Boundary conditions given on the cutting groove.

The application range of Matsuyama et al.'s [37] analysis is limited to two-dimensional linear problems. For that reason, these results cannot be directly applied to the analysis of oxy-fuel gas cutting where a temperature gradient in the through thickness direction is generated due to the heat transmitted from the preheating flame. In this study, Matsuyama's method is modified so that the temperature dependency of the thermomechanical properties and the temperature gradient in the thickness direction can be taken into consideration during the gas cutting simulation.

2.3.2 Heat conduction analysis using a moving coordinate system

Consider the case where a fixed speed torch is aligned above a steel plate. Fixed coordinates (x, y, z) are placed on the steel plate, with the xy plane in the steel plate plane. The elapsed time from the start of calculation is expressed as t and the xy component of the speed vector of a torch moving in the xy plane as (u, v) . Finite element analysis of heat conduction using fixed coordinates [38] is performed by the following procedures.

- a) Let torch's xy coordinates and temperature field, at time to be (x_0, y_0) and $T_0(x, y, z)$. Eq. (2.6) is solved, for given time increment Δt and the thermal boundary conditions around the torch centered on (x_0, y_0) . The temperature $T_1(x, y, z)$ at the new time $t_1 = t_0 + \Delta t$ is calculated by Eq. (2.6).

$$[K]\{T\} + [C]\{\partial T/\partial t\} = \{F\} \quad (2.6)$$

where $[K]$ is the heat conduction matrix, $[C]$ the thermal capacity matrix, $\{F\}$ the heat flux vector, $\{T\}$ the nodal temperature, and $(\partial T/\partial t)$ the changing rate of temperature.

- b) With the torch coordinates at the new time being $(x_0 + u\Delta t, y_0 + v\Delta t)$, the heat boundary conditions are updated.

In procedure b), when the torch position is unchanged at (x_0, y_0) , $T_1(x - u\Delta t, y - v\Delta t, z)$ is given as the present temperature at positions (x, y, z) . This makes it possible to carry out heat conduction analysis using a moving coordinate system fixed to the torch. When the workpiece is of finite dimensions, a domain which was not in the finite element model appears in Δt , at the edge in front of the torch, and the model has to be extended behind the torch.

A schematic view of the model is shown in Fig. 2.4. The moving coordinate system (ξ, η) and the fixed coordinate system (x, y) are defined on the workpiece. The torch velocity in the (x, y) system is (u, v) , the torch position in the (ξ, η) system is (O_ξ, O_η) and the norm of vector (u, v) is $|v|$. (O_ξ, O_η) is unchanged over time and the temperature fields move in parallel by $(-u, -v)$ in a unit time. This vector is referred to as ‘temperature field movement velocity’. The distance of torch movement up to time t is $|v|t$.

The distance ψ is defined as shown in Fig. 2.4. $\psi < 0$ in front of the torch, and $\psi > 0$ to its rear. As described by Osawa et al. [30], there is a significant temperature rise within the domain $-(16\tilde{k})/|v|^2 \leq \psi \leq 0$ in front of the torch. The ψ (a negative value) at the model’s front end of this domain is called ‘fore’ and the ψ (a positive value) at the model’s rear end is called ‘aft’. ‘aft’ increases with t . Let ‘aft’ at $t = 0$, calculated finish time t_E and time t be aft_0, aft_E, aft_t .

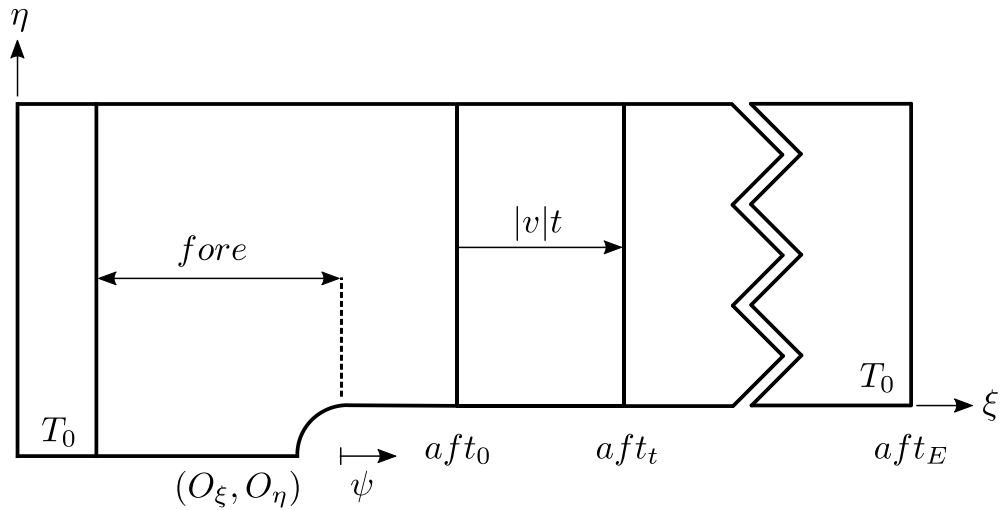


Fig. 2.4 A finite plate model for transient heat conduction analysis using moving coordinates.

When the model's front end is more distant from the torch than $|fore|$, there is no temperature increase in the newly generated area. Room temperature is given to the nodes in this region. The model is prepared up to aft_E . At $t = 0$, elements with $\psi > aft_0$ are killed (i.e. the thermal conductivity is set to a negligible value). When the time changes from t to $t + \Delta t$, the elements with $aft_t \leq \psi \leq aft_{t+\Delta t}$ are born. The temperatures at a calculation point of the newly-born elements are then given as the temperature at $\psi = aft_t$.

2.3.3 Translation of the temperature field

In an analysis using the moving coordinates described in Section 2.3.2, the moving coordinate system (ξ, η) in the plate and the fixed coordinate z in the plate

thickness direction are combined to give the locations of the calculations points. During the analysis, the temperature field $T_1(x, y, z)$ shows translational movement to the same extent as the torch displacement $(u dt, v dt)$ in Δt . Thus, the initial value of the time integration of the temperature at (ξ, η, z) is given by the temperature at $(\xi - u\Delta t, \eta - v\Delta t, z)$ at t . The detail of the time integration procedure is explained in Osawa et al. [30].

2.3.4 Two-dimensional surface temperature field

Let ‘evaluation plane’ $\pi(z)$ be the plane parallel to the heating face with the thickness coordinate of z . For the three-dimensional heat conduction analysis, the provisional temperature distribution on $\pi(z)$ is given by the analytical method proposed by Matsuyama et al. [37]. In these calculations, the uniform tentative length of S_2 boundary (see Fig. 2.3) is given to all evaluation planes.

2.3.5 Three-dimensional temperature field

The work-piece’s three-dimensional temperature distribution during oxy-hydrogen cutting process can be calculated by performing a three-dimensional finite element (3D-FE) moving coordinate quasi-stationary heat conduction analysis, with the heat flux of the preheating flame estimated in Section 2.2 and the provisional kerf temperatures given in Section 2.3.4

The use of moving coordinates facilitates a finite element discretization which faithfully expresses the groove shape and also it prevents the accuracy deterioration in the heat input estimation caused by rapid changes in thermal boundary conditions, without the need for expressing the melting of the cut metal in terms of element death.

However, the provisional kerf temperatures given in Section 2.3.4 are calculated without the consideration of the temperature gradients in the thickness direction due to the preheating, the temperature dependencies of thermal material properties are ignored, and the uniform length of S_2 boundary chosen in Section 2.3.4. is unrealistic. Apparently, the accuracy of the calculated three-dimensional temperature field is not expected. As described later, a sharp temperature discontinuity on the border between S_2 (prescribed non-uniform temperature) and S_3 (adiabatic boundaries is calculated in the 3D-FE solution.

It is needed to adjust the kerf temperature on each $\pi(z)$ in order to reduce this temperature discontinuity, and achieve a heat conduction field which is consistent with the temperature gradient in the thickness direction due to preheating, and the non-uniform thermal conditions for the groove leading edge and rear side kerf.

2.3.6 Three-dimensional temperature field adjustment

As shown in Fig. 2.3, boundaries S_1 - S_3 are set on each evaluation surface $\pi(z)$. Let F be the intersection between the heating line center and the groove's leading edge, s the gauged path length along the groove from F , l_1 and l_2 the length of S_1 and S_2 boundaries. Let $T(s, z)$ be the kerf temperature at a distance s on $\pi(z)$.

During gas cutting, a temperature gradient along the thickness direction is caused by the preheating flame. Accordingly, the kerf temperature distribution on each $\pi(z)$ is modified by the following procedure, and they are adopted as the thermal boundary condition for three-dimensional analyses. Because the temperature on S_1 equals the melting point and the S_3 is adiabatic, temperature modification is only required in the S_2 boundary. Let $T_{2D}(s)$ be the two-dimensional temperature distribution at distance s from F determined by Matsuyama's method [37], and $T_{3D}(s)$ be the temperature calculated by the 3D-FE analysis in which $T_{2D}(s)$ is given as the S_2 boundary condition.

Fig. 2.5 illustrates the kerf temperatures on S_2 and S_3 boundaries. ξ and η are distances from the torch center measured in the cutting direction and the transversal direction. Osawa et al. [30] reported that, when $\pi(z)$ is close to the heating face, $T_{3D}(s)$ becomes higher than $T_{2D}(s)$ on S_2 , and a sharp discontinuity arises on the

S_2/S_3 border when the provisional kerf temperatures given in Section 2.3.4 are applied.

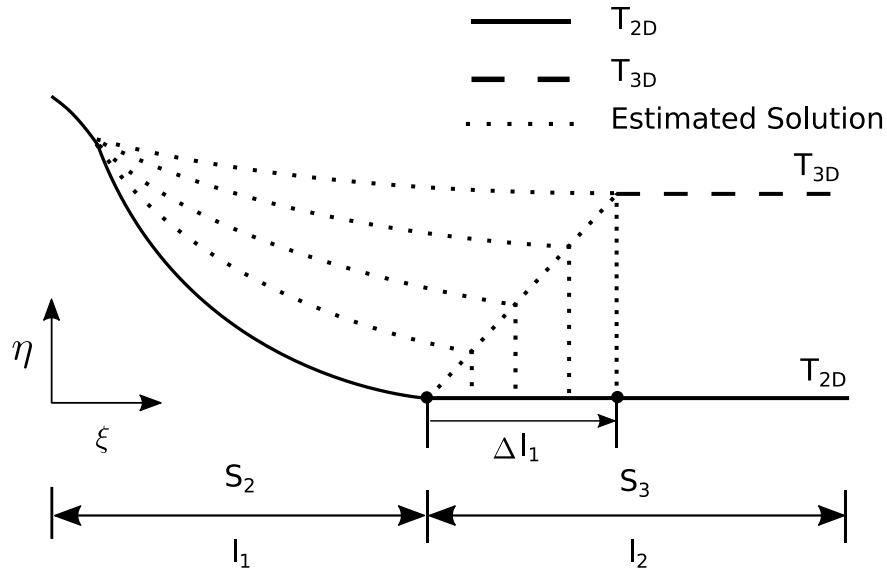


Fig. 2.5 Schematic view of the temperature distribution at the heating face.

The S_2 length (l_1 in Fig. 2.3) chosen in the provisional analysis is a tentative value, and it can be changed. Let $l_1 + \Delta l_1$ be the modified S_2 length. $T_{2D}(s)$ is re-analyzed for this updated S_2/S_3 configuration. When this updated $T_{2D}(s)$ is applied in 3D-FE analysis, the updated $T_{3D}(s)$ on S_2 becomes higher than that before the updating, and the discontinuity becomes less significant (see Fig. 2.5). Adjusting Δl_1 on each $\pi(z)$ by trial and error, the optimized three-dimensional S_2/S_3 configuration,

for which the temperature discontinuity on the S_2/S_3 border is negligible on all $\pi(z)$, can be determined.

2.4 Conclusions

The theory and methods considered in the numerical models are described in this chapter. The heat transfer parameter estimation is carried out by employing the method developed by Osawa et. al [12]. During the gas cutting simulation, the kerf temperature is analyzed based on the numerical method developed by Matsuyama et al. [37]. The three dimensional temperature distribution during the cutting simulation is calculated by performing a three-dimensional finite element moving coordinate quasi-stationary heat conduction analysis. A technique for the estimation of the three-dimensional temperature fields considering inclined cutting fronts is proposed. The ratio of the preheating heat input and the material combustion heat input is then examined by performing moving coordinate quasi-stationary finite element heat conduction analysis implementing the proposed technique.

Chapter 3

Experimental Tests

3.1 Introduction

In order to quantify the effects of the preheating flame state on the oxy-hydrogen cutting performance, a series of experiments were carried out during this study. In order to identify the heat transfer parameters during the oxy-hydrogen cutting process, spot heating test for the preheating gases H_2 , H_2-CO_2 and H_2-AR are performed. The accuracy of the identified heat transfer parameters is then validated with the results of piercing test of the selected gases.

Additionally, cutting tests are carried out in order to measure the effects of the selected preheating gases on the geometry of the cut during the oxy-hydrogen cutting process. All the information gathered from the experiments is then implemented in the three-dimensional gas cutting simulation. In the following sections, the description of the experimental tests and the results are detailed.

3.2 Spot Heating Test

3.2.1 Experimental setup

Spot heating test are conducted to identify the heat transfer characteristics of the preheating flame. A mild steel circular plate of 6 mm thickness and 300 mm diameter is placed horizontally and a cutting nozzle is positioned at the center of the plate with a standoff distance of 6 mm, as shown in Fig. 3.1. A set of thermocouples are placed at the back surface to record the temperature distribution on the plate during the trials, and heat insulation material is used to coat the back of the plate.

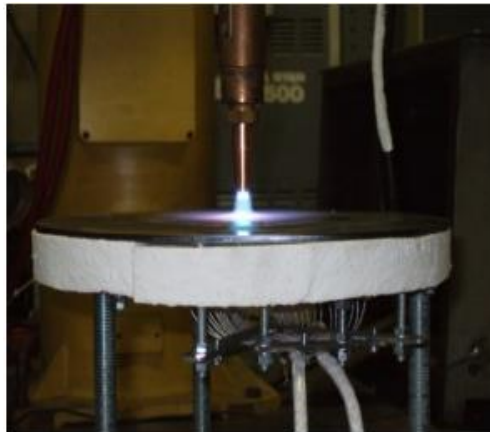


Fig. 3.1 Test specimen used during the spot heating trials.

In order to evaluate the influence of the preheating flame composition on the cutting performance, five different preheating flames are selected for the trials. Pure H₂ (reference preheating flame) and a gas mixture of H₂ with CO₂, and H₂ with AR in different mixing ratios are prepared for the test. The preheating flame conditions of each preheating flame is show in the Table 1.

Nissan Tanaka 3055B D5 No. 4 LPG divergent nozzle [39] as shown in Fig. 2.2(b), was employed in all heating tests. This nozzle is suitable for cutting of steel plates with a thickness up to 25 mm. The distance from the nozzle center to the exit of the preheating gas spouts, R_0 is 2.7 mm.

Table 3.1 Preheating gas flame composition

Preheating Gas	100%H₂ -0%CO₂	90%H₂- 10%CO₂	80%H₂- 20%CO₂	90%H₂- 10%AR	80%H₂- 20%AR
Standoff distance [mm]	6	6	6	6	6
Pressure of Hydrogen [MPa]	0.105	0.104	0.103	0.104	0.104
Flow of Hydrogen [l/min]	29	29	29	29	29
Flow of Oxygen [l/min]	6	6	6	6	6
Flow of CO ₂ [l/min]	0	3	7	0	0
Flow of AR [l/min]	0	0	0	3	7

The temperature distribution at the back face was measured using chromel-alumel thermocouples (Type-K) with sheath diameter of 0.1 mm fitted in both perpendicular directions from the center. As shown in Fig. 3.2, the thermocouples were fitted using percussion welding. A pitch of 2 mm was used from the plate center up to 12 mm, then a 4 mm pitch was used from 12 mm up to 40 mm, and finally, a pitch of 8 mm was used on the periphery of the plate; 26 mm thick steel wool was stretched over the backface of the plate. During the trials, the thermocouple output was recorded for 5 s at intervals of 0.2 s once the heating torch had been placed in the center of the plate. The movement of the torch was controlled by Daiden Fanuc ARC Mate DR-400 welding robot. The heating time for the tests is fixed to 6 seconds, after that the torch is immediately removed from the plate so that the plate starts to cool down.

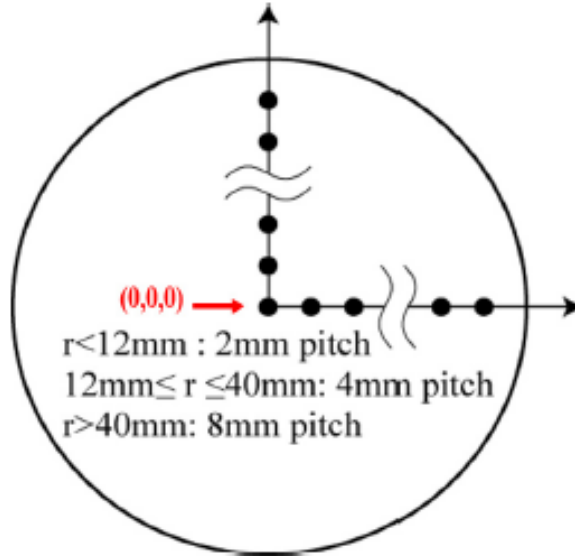


Fig. 3.2 Thermocouples arrangement employed for the spot heating tests.

3.2.2 Results

The comparison of the temperature history at the plate back surface from 100%H₂, 90%H₂-10%CO₂, 80%H₂-20%CO₂, 90%H₂-10%AR, and 80%H₂-20%AR is shown in Fig. 3.3. From the figure can be shown that the highest back surface temperature is obtained with 100%H₂. By comparing the AR mixing ratios, it is observed that as the ratio of AR increase, the temperature at the plate back face decreases. In the same manner, by comparing the CO₂ mixing ratios, it is observed a decrease in the temperature with the increase of the CO₂ mixing ratios. On the other hand, by comparing the employed added gas, it is observed that the back face temperature of the AR trials is higher than the CO₂ trials.

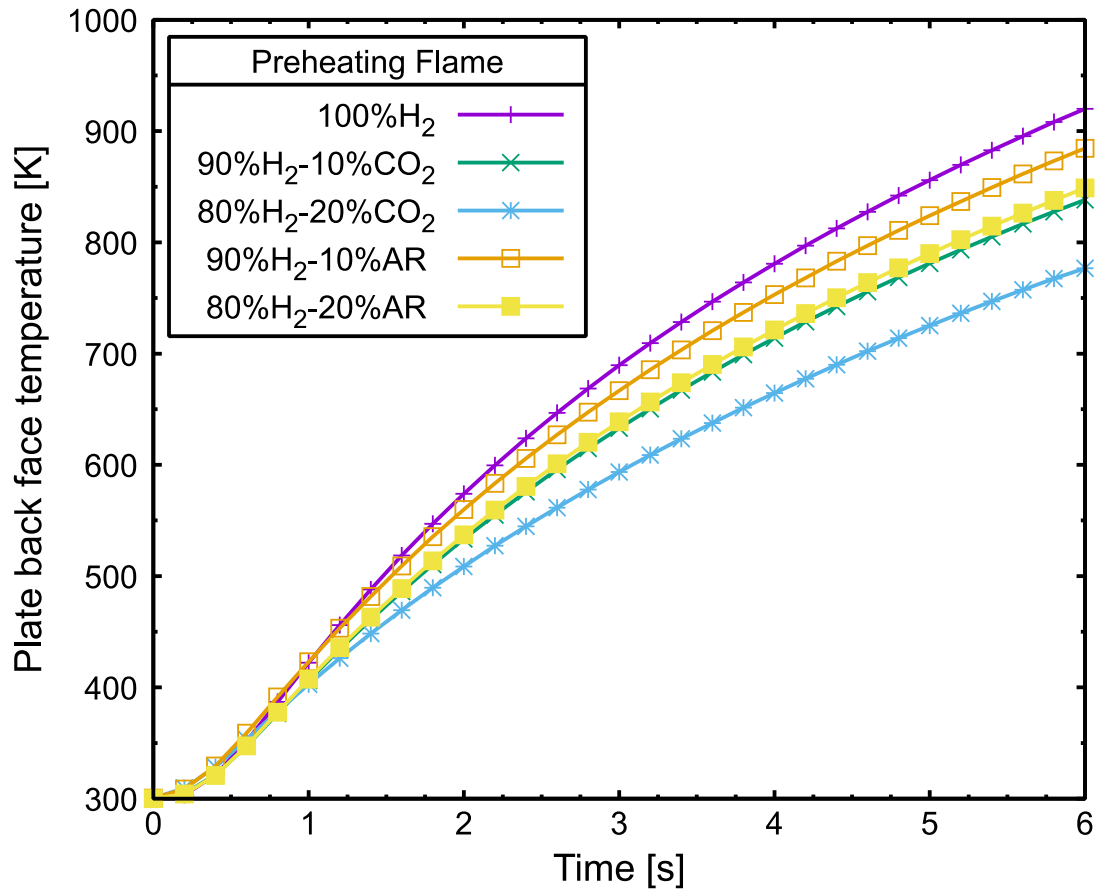


Fig. 3.3 Back surface temperature recorded at the center of the plate.

3.2.3 Discussion

From the Fig. 3.3, it is clearly shown that the temperature measured in the disk is influenced by the gas mixing ratio as well as the employed added gas. However, it is not clear the reason for this temperature drop.

3.3 Piercing Tests

3.3.1 Experimental setup

A rectangular steel plate of 12 mm thickness is arranged horizontally, a cutting nozzle is positioned above the plate with a standoff distance of 6 mm, as shown in Fig. 3.4. The employed thickness during the tests is comparable to the cutting nozzle recommended thickness. The temperature distribution over the plate is measured by a thermal camera FLIR SYSTEM SC620 NTSC placed about 1.5 m away from the workpiece. The piercing conditions used in the trials (nozzle, preheating flame, torch movement) are the same as those used during the spot heating tests.

(a)



(b)



Fig. 3.4 Test specimen employed during the piercing test. (a) succeed piercing test.
(b) failed piercing test.

As a prerequisite for the piercing process, the workpiece must reach its kindling temperature contrarily, the piercing fail. To ensure that the heated surface reaches the after mentioned temperature the preheating time for the first piercing test is fixed to 23 seconds. Then, the piercing process on the workpiece is evaluated to determine whether the plate pierced or not. For the second trial, the preheating time decreased by 3 seconds and the piercing process is evaluated once again. This preheating time reduction method continues until the piercing process fails during the last trial. Table 3.2 shows the summary of the piercing tests.

Table 3.2 Measured piercing times when employing 100%H₂ preheating flame.

Preheating Gas	Preheating Time [s]	Plate Piercing
100%H ₂	14	Failed
	17	Succeed
	20	Succeed
	23	Succeed

From Table 3.2 is observed that the minimum piercing time falls between the range $14 < t < 17$ seconds, when the preheating flame 100%H₂ is employed. It is observed that the diameter of the area in which the temperature exceeded the steel's kindling temperature (about 1300 K) at the end of the preheating was larger than 6 mm for the cases where the plate was pierced.

3.3.2 Results

Table 3.3 shows the measured t_{min} during the tests for the selected preheating flames. From the table is observed that the shortest t_{min} is obtained when employing 100%H₂ preheating flame. On the other hand when employing 80%H₂-20%CO₂, t_{min} is increased around 40 seconds.

Table 3.3 Estimated minimum piercing times

Preheating Flame	Measured Minimum Piercing Time [sec]
100% H ₂	13
90% H ₂ -10% AR	25
80% H ₂ -20% CO ₂	53

3.3.3 Discussion

The obtained results, clearly shows the negative impact of the AR and CO₂ in the piercing time of the oxy-hydrogen cutting process. The obtained results support Ikegami's claim that the cutting deteriorates when CO₂ is mixed into the preheating gas. However, the reason of this deterioration whether is produced by the preheating heat input or the material combustion heat input cannot be clarified.

3.4 Gas Cutting Tests

3.4.1 Experimental setup

Oxy-hydrogen gas cutting test for thick steel plate was performed. The preheating gas conditions shown in Table 3.1, which are the same as those for the spot heating test in Section 3.2. Based on the results of the piercing test, the gas

cutting test is devoted to analyze the influence of the 100% H_2 and 80% H_2 -20% CO_2 preheating flames.

Fig. 3.5 shows the shape and size of the specimens. That is mild steel (SS400) rectangular plate with length 200 mm x width 100 mm x thickness 25 mm. The mill scale was not removed before cutting. Let x and y be the longitudinal and transversal coordinates on the plate. The origin is set at the model end on the center line. A 10 mm diameter hole was opened using a drill at the point with $(x, y)=(25 \text{ mm}, 0 \text{ mm})$. Heating is carried out along the x -axis, starting at the drill hole ($x = 25 \text{ mm}$) and ending at $x = 145 \text{ mm}$. During the trials, the specimens were not pierced before the cutting. The cutting speed V was set to 5 mm/sec for both preheating flames. For all the cutting test performed in this study, the cut face quality met the best grade (Grade 1) of JWES WES2801 (quality standard for gas cut surface) [40]), and there was no dross adhesion.

Let d , be the groove width at the mid-point of the cutting line (see Fig. 2.3), a be the groove's half width ($d/2$), 'groove tip' be the intersection between cutting center line and the leading edge (point F in Fig. 2.3), λ be the ratio of groove diameters in x and y directions (see Fig. 2.3) and κ the measure of the drag. (see Figs. 3.5). Once the cutting process finished, d was measured, and then the specimen was cut along the centerline in order to measure the groove's leading edge shape.

On this cut surface, x-coordinates of groove tips on the front and backface were measured, and the drag κ was calculated.

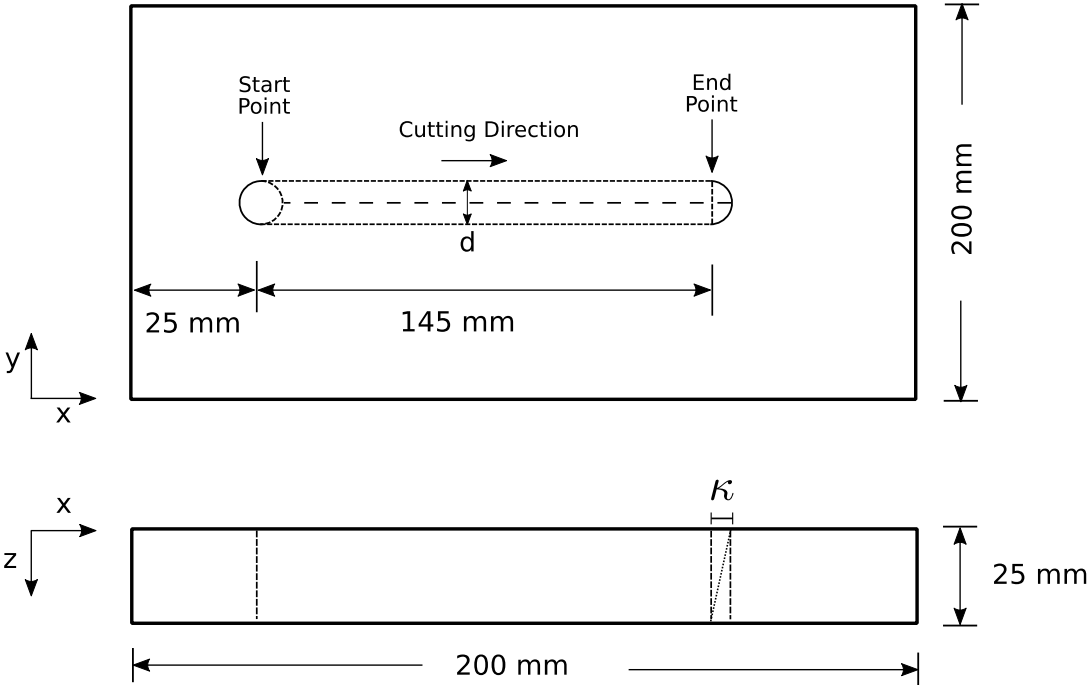


Fig. 3.5 Steel plate specimen used during the cutting test.

3.4.2 Measurement results

The steel plate specimens employed during the cutting tests are shown in Fig. 3.6, and the shape parameters (d , κ , λ) are shown in Table 3.4. The side view of the cutting kerf is shown in Fig. 3.7. From the table can be observed that, for the selected cutting speed, there is no significant difference in the groove shape and size.

However, a significant difference is observed in the drag when employing 80% H_2 -20% CO_2 .

3.4.3 Discussion

The obtained results show a clear deterioration in the cut quality when employing 80% H_2 -20% CO_2 . This deterioration agrees with the results obtained during the piercing test. Moreover, the results show that for the numerical simulation of the oxy-hydrogen cutting process the cutting front inclination must be considered during the analysis.

Table 3.4 Summary of the gas cutting test results.

Preheating Gas	100%H_2- 0%CO_2	80%H_2- 20%CO_2
Plate thickness h [mm]	25	25
Cutting speed V [mm/s]	5	5
Cutting-front drag κ [mm]	1	3.5
Groove width d [mm]	3	3
Ratio of groove diameters λ	1.0	1.0

(a)



(b)



Fig. 3.6 Steel plate specimen cutting groove. (a) 100%H₂-0%CO₂. (b) 80%H₂-20%CO₂.

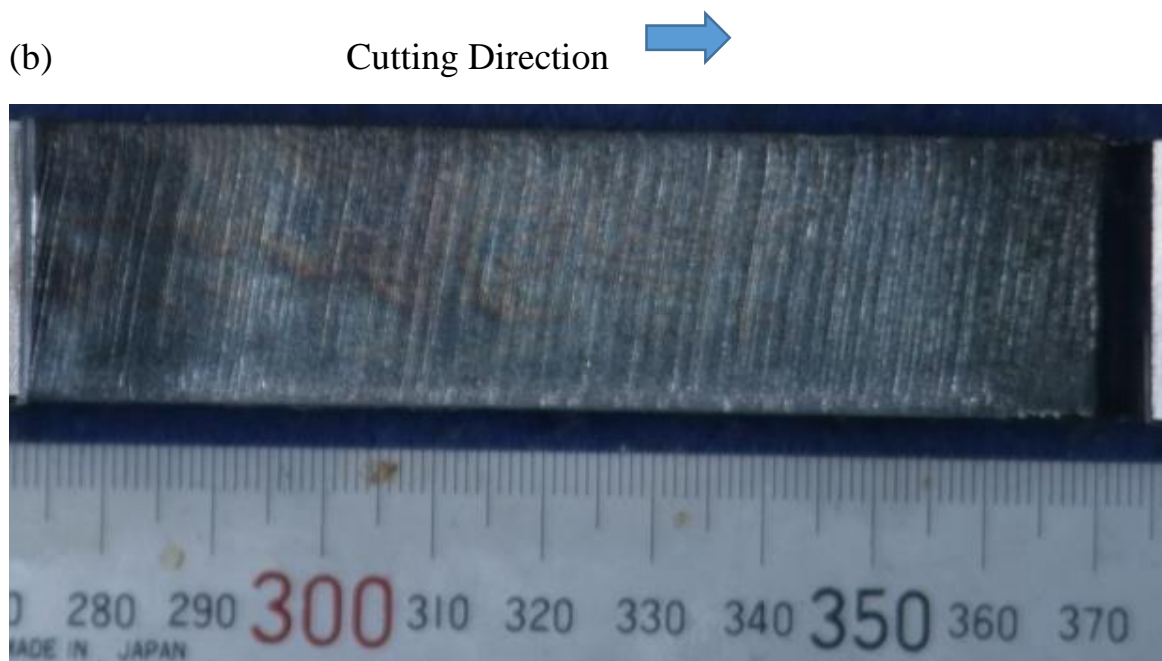
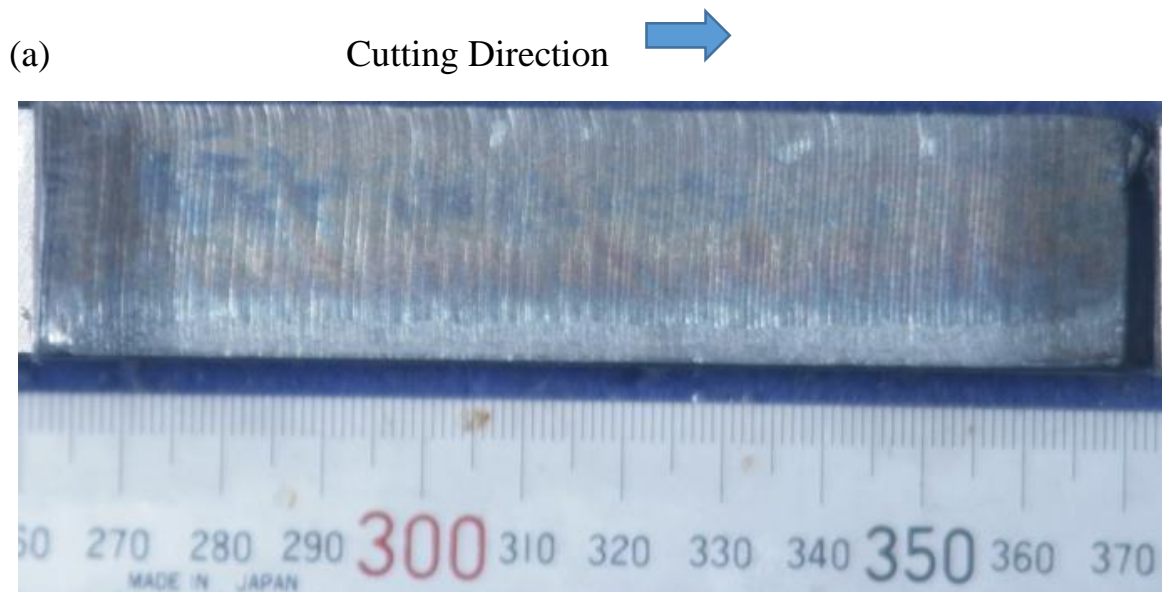


Fig. 3.7 Steel plate specimen kerf side view. (a) 100% H_2 -0% CO_2 . (b) 80% H_2 -20% CO_2 .

3.5 Conclusions

In order to quantify the effects of the preheating flame state on the oxy-hydrogen cutting performance, spot heating tests as well as piercing process test, and gas cutting test were carried out. The results from the experimental tests can be summarized as follow:

Spot heating tests:

- The highest back surface temperature is obtained when employing 100%H₂ preheating gas.
- By comparing the mixing ratio of the added gases (AR and CO₂), as the mixing ratio increases, the measured temperature at the back-face decreases.
- By comparing the employed added gas (AR and CO₂), the measured temperature of the AR trials was higher than the CO₂ trials.

Piercing test:

- The obtained results show a clear deterioration in the cutting performance when employing 80%H₂-20%CO₂. The shortest minimum piercing time t_{min} (13 secs), is obtained when employing 100%H₂. In contrast, when employing 80%H₂-20%CO₂ the minimum piercing time is increased by 40 secs.

Gas cutting test:

- The obtained results show a clear deterioration in the quality of the cut. The measurements of the cutting test specimens show an important increase in the drag when employing 80%H₂-20%CO₂

Chapter 4

Numerical Simulation of the Piercing Process

4.1 Introduction

In the present study, to analyze the influence of the preheating flame characteristics on the cutting performance, the piercing process is numerically simulated by employing the heat transfer parameters identified from the spot heating test. Since during the oxy-fuel cutting process, the heat transferred from both the preheating flame and that from the material combustion arises at once, it is challenging to simulate the cutting process numerically. However, by studying the piercing process, the thermal effects can be analyzed.

4.2 Identification of Heat Transfer Parameters

4.2.1 Model description

A direct heat conduction analysis is performed by using an in-house axisymmetric thermal finite element code developed by Osawa et al. [12]. $Y_{J,K}$ in Eq. 2.5 are calculated by carrying out axisymmetric finite element direct heat conduction analyses in which $T_G(r)$ and $\alpha(r)$ represented by Eqs. 2.2, 2.3 and 2.4 are applied as boundary conditions.

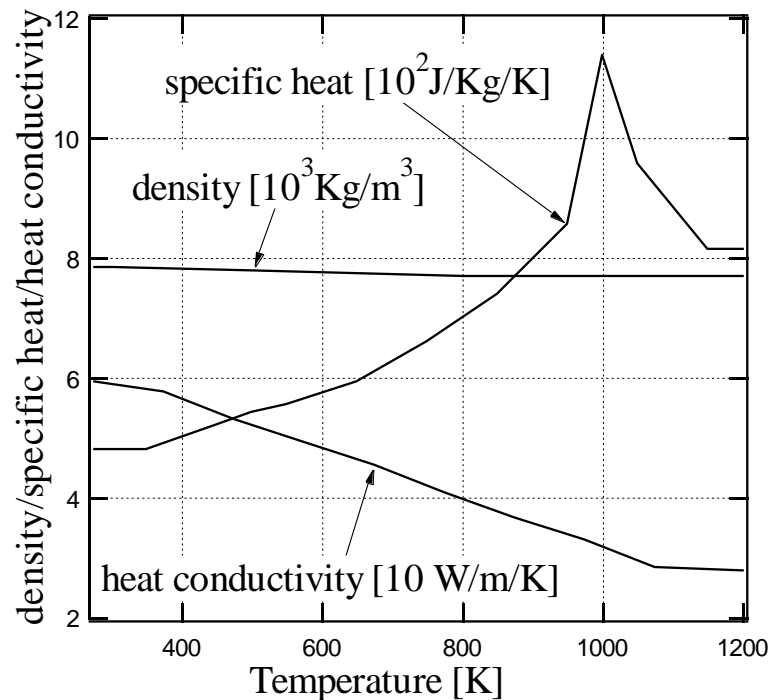


Fig. 4.1 Temperature dependency of the material properties.
(from Osawa et al. [12])

The temperature dependencies of the material properties employed during the analyses are shown in Fig. 4.1. The model comprises 4 node isoparametric quadrilateral elements, and the back surface is assumed to be adiabatic. A finite element mesh is prepared based on the thin circular plate geometry used in the spot heating test. The employed mesh and its dimensions are presented in Fig. 4.2 and Table 4.1. The initial temperature of the analysis is set to 300 K. The convective heat transfer between plate and air is evaluated at the outer end, and its coefficient is 480 W/(m²K).



Fig. 4.2 Finite element mesh employed during the heat conduction analyses.

Table 4.1 Finite element model dimensions

Model dimensions [m]	0.3 x 0.006
Number of elements (x, y, z) axis	40 x 40 x 6
Max./Min element size on x-axis [m]	(3.44/13.8) x 10 ⁻³
Max./Min element size on y-axis [m]	(3.44/13.8) x 10 ⁻³
Max./Min element size on z-axis [m]	(5.04/16.8) x 10 ⁻³

The genetic algorithm analyses are performed by the Design Analysis Kit for Optimization and Terascale Applications (Dakota) open source software [41]. The genes $d_c, d_0, d_E, e_c, e_0, e_E, f_1, g_1, f_2, g_2, \dots, h_1, k_1, h_2, k_2, \dots$ are optimized so that E in Eq. 4 is minimized by Self-Adaptive-Evolution Algorithm [42].

The control points are arranged at $r= 1.2, 1.6, 1.8$ inside the inner region, and at $r= 4.28, 7.32, 13.4, 21.0$ and 32.4 mm inside the outer region. As reported by Osawa et al. [12], T_G and α between the control points are estimated by linear interpolation because the difference in the calculated back face temperatures derived from spline interpolation and that from linear interpolation is negligible.

4.2.2 Estimation of heat transfer parameters

In this study, T_G and α around the torch center were identified from the measured back face temperatures following the inverse heat conduction analysis method explained in Section 2.2. The comparison of the T_G distributions for the chosen preheating flames are shown in Fig. 4.3.

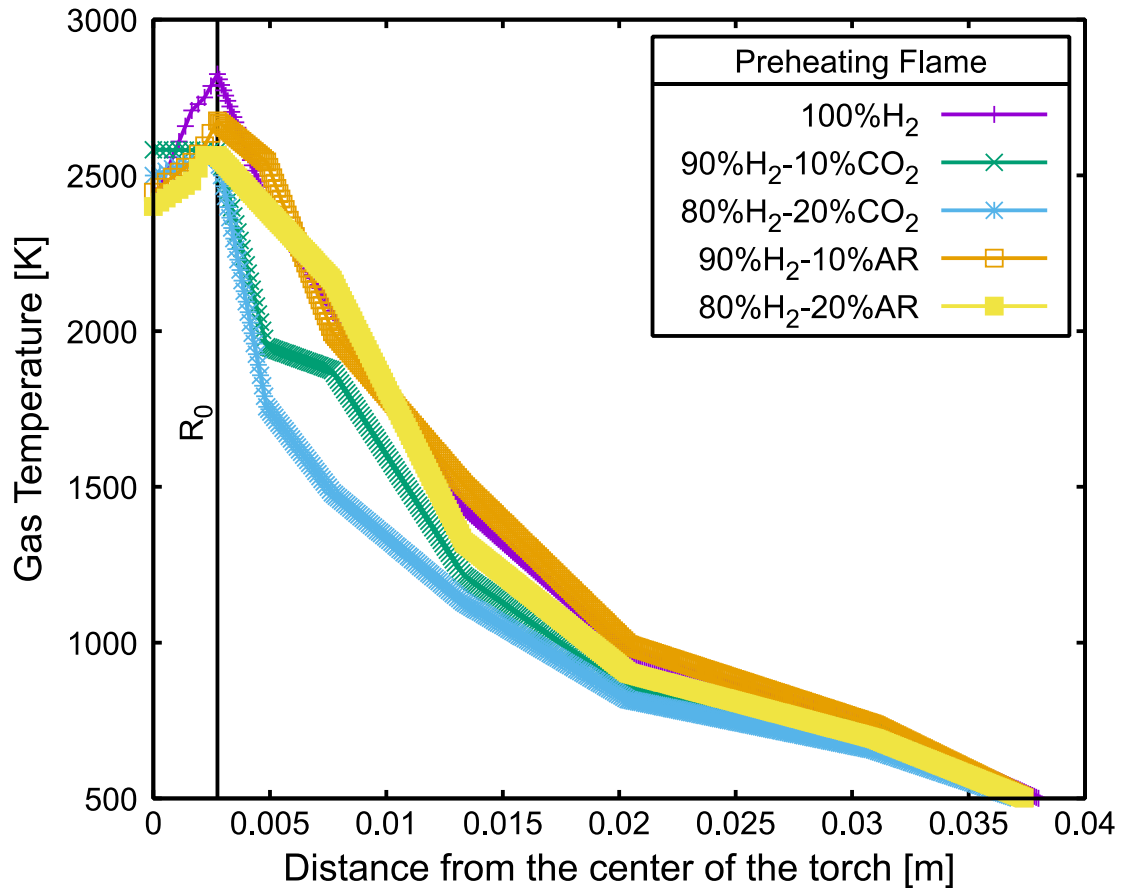


Fig. 4.3 Comparison of the estimated gas temperature.

From the figure can be observed that the highest T_G is obtained for 100% H₂, just below the spout (R_0). By comparing the AR mixing ratios, it is observed that as the ratio of AR increase, the temperature at the plate back face decreases. On the other hand, by comparing the CO₂ mixing ratios, it is observed that as the ratio of CO₂ increase, the temperature at the backface decreases. By comparing the employed gases, it is observed that the backface temperature of the AR trials are higher than the CO₂ trials. Moreover, it is observed that the temperature in the outer skirt

becomes significantly lower for the CO₂ trials while AR trials shows a similar behavior as the 100%H₂ trials. As shown in Fig. 4.3, while the increase of the AR mixture ratio has a small impact on the estimated gas temperature, the increase of the CO₂ mixture ratio has a significant impact on the gas temperature.

In addition to the gas temperature, α distribution for the chosen gases is presented in Fig. 4.4. The figure shows the heat transfer coefficient is at its maximum below the combustion flame exit for all the chosen gases. In addition, a substantial decrease in the α distribution near the combustion spout its observed. For example, when $r = 0.01$ the transfer coefficient is around 1900 for CO₂ and around 1700 for AR.

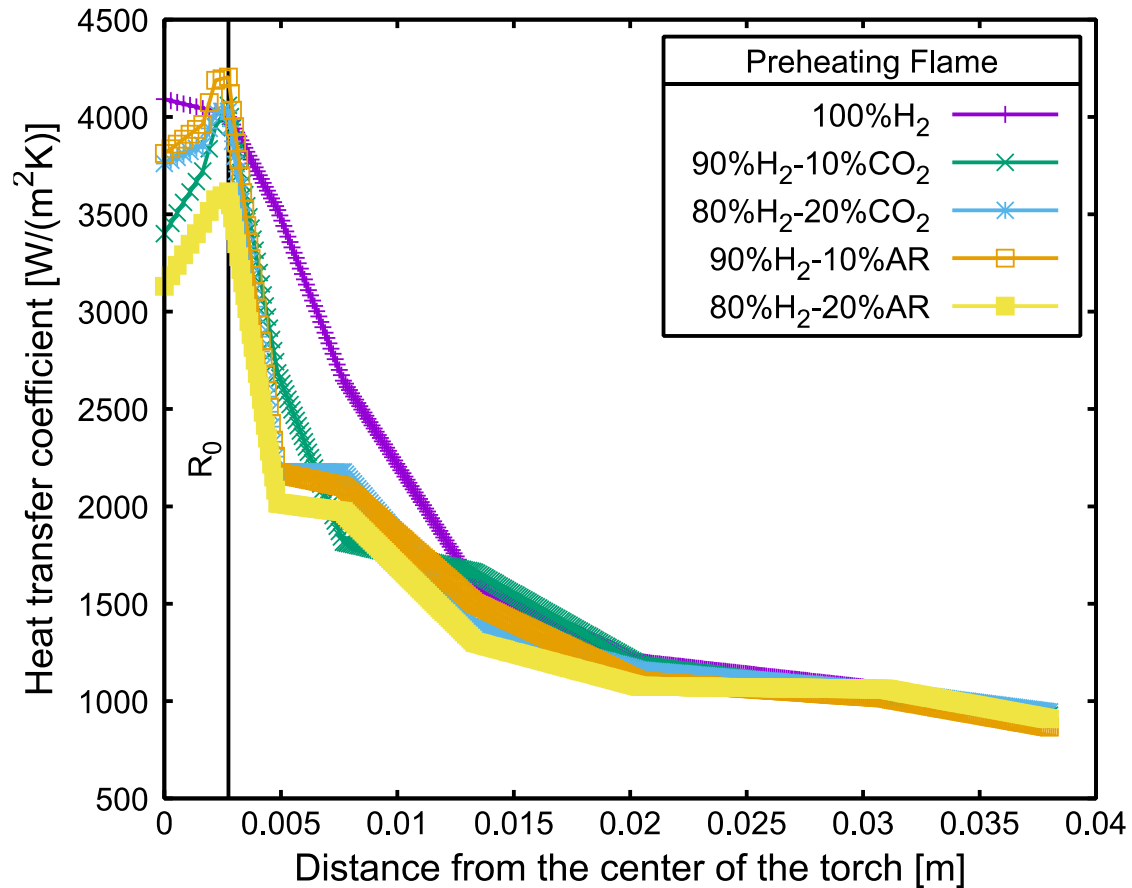


Fig. 4.4 Comparison of the heat transfer coefficient.

From these findings, it seems evident that, the reduction of the heat transfer coefficient for both the AR and CO₂ is almost same while the gas temperature of the AR mixture is similar to 100% H₂ but for the CO₂ trials, not only the transfer coefficient but also the gas temperature declines.

To examine the accuracy of the identified parameters, a direct heat conduction analysis is performed by an FE code that employs the identified heat transfer

parameters to estimate the back face temperature of the plate during the spot heating test. Figs. 4.5 to 4.9 shows the temperature over time of the thermocouples located at a distance $r = 4, 6, 8, 10$ and 12 mm, from the center of the plate for all the preheating flame conditions of the spot heating tests. The comparison of the back face temperature between the FE code analysis (Estimated) and the recorded from the spot heating test (Experiment) shows the accuracy of the identified heat transfer parameters.

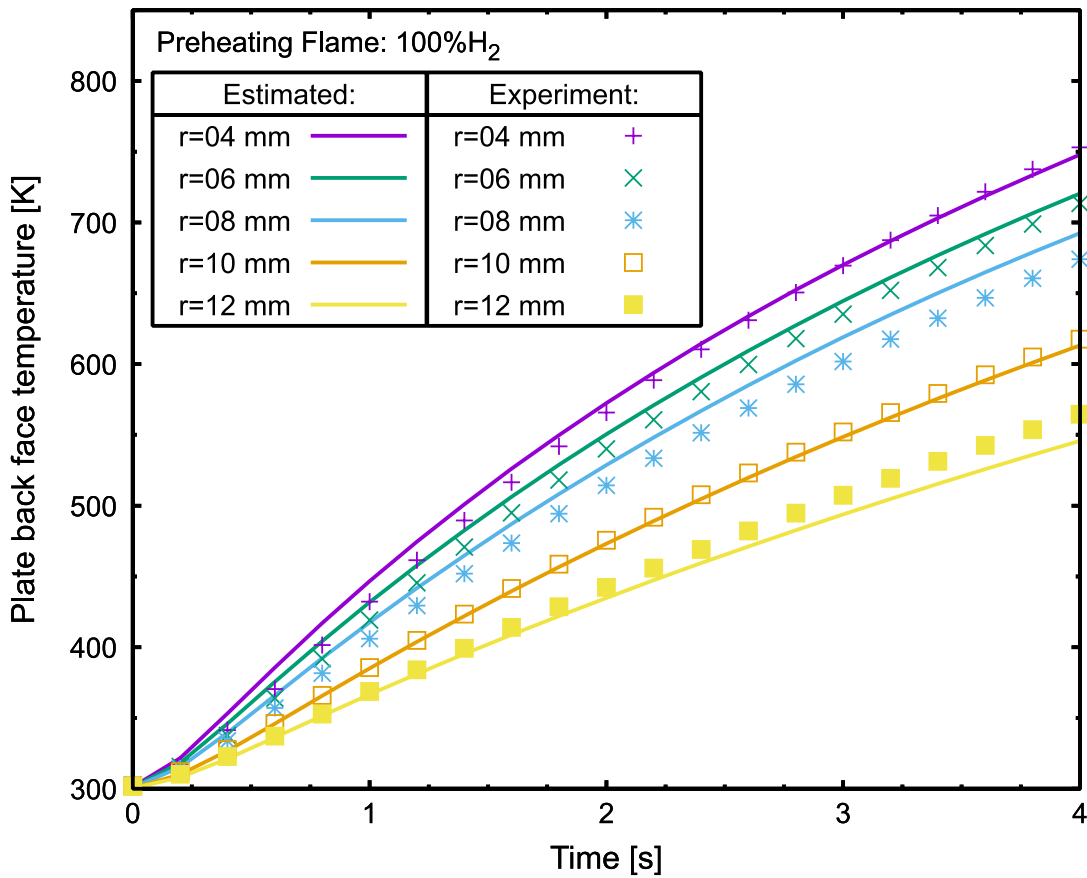


Fig. 4.5 Comparison of the estimated and experimental back face temperature for 100%H₂.

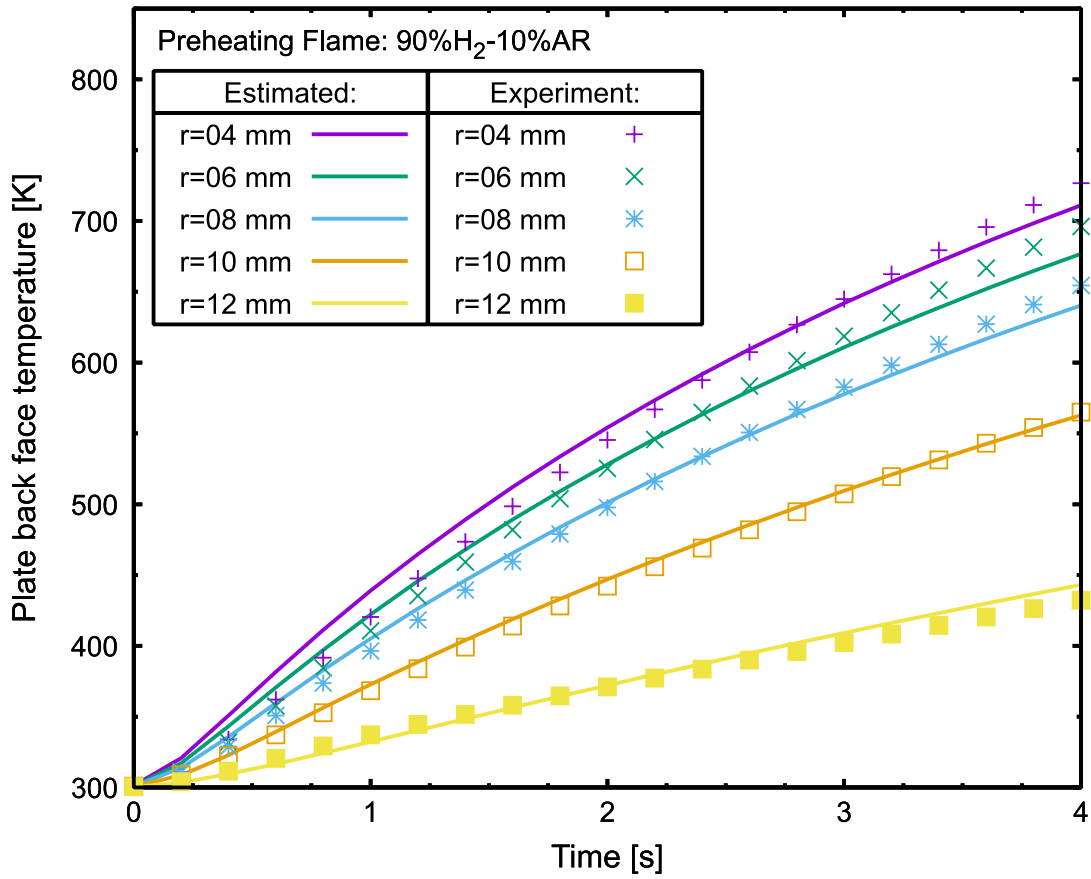


Fig. 4.6 Comparison of the estimated and experimental back face temperature for 90%H₂-10%AR.

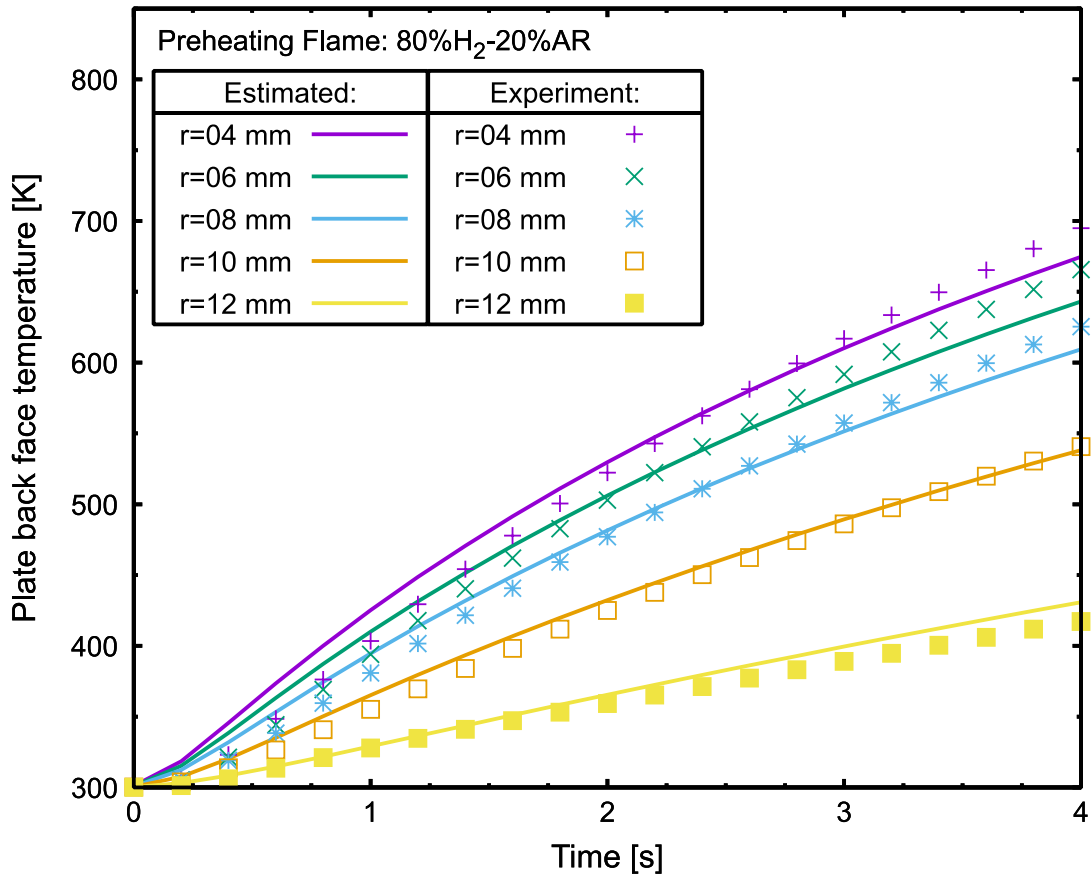


Fig. 4.7 Comparison of the estimated and experimental back face temperature for 80% H₂-20% AR.

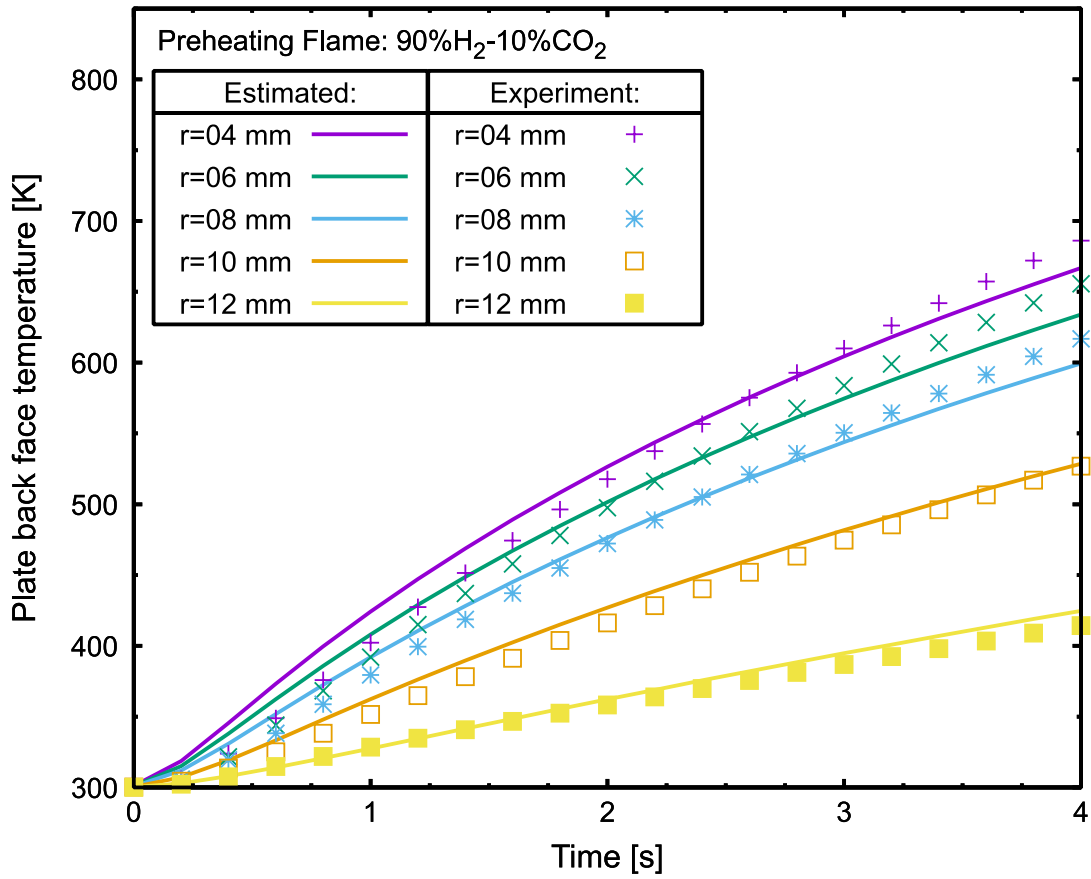


Fig. 4.8 Comparison of the estimated and experimental back face temperature for 90% H_2 -10% CO_2 .

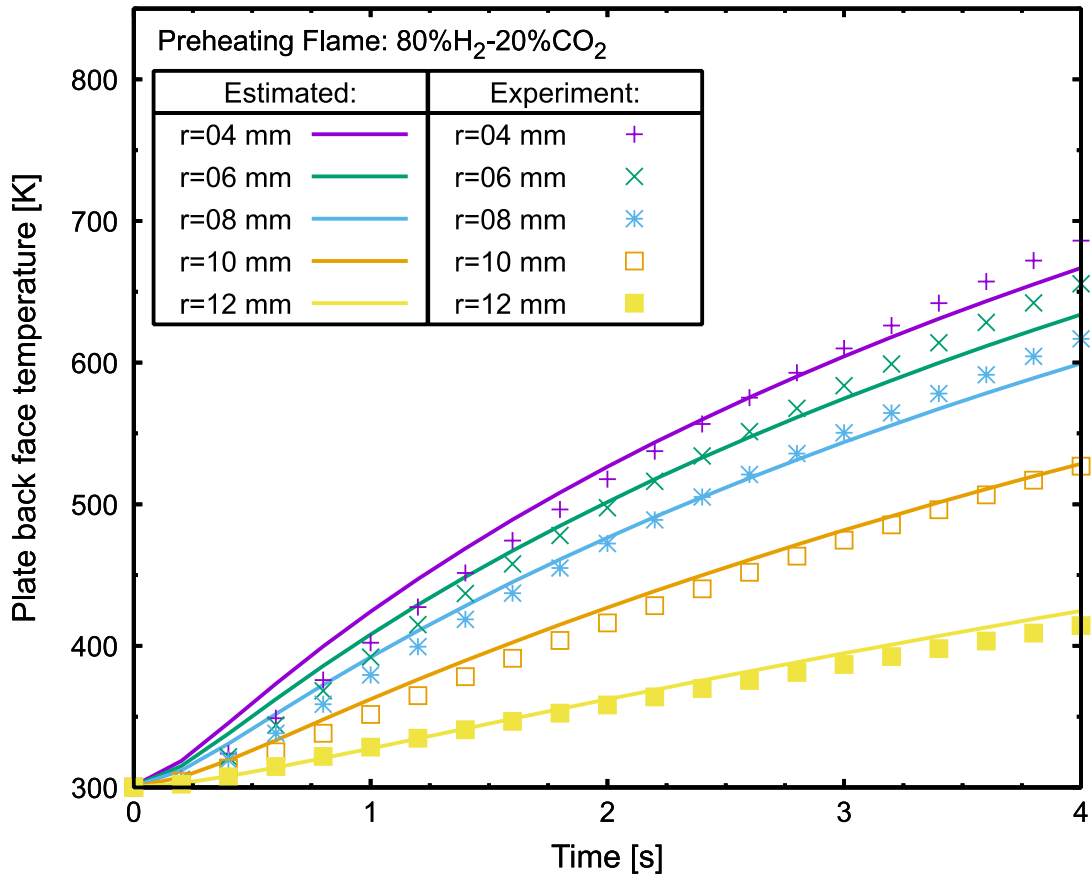


Fig. 4.9 Comparison of the estimated and experimental back face temperature for 80% H₂-20% CO₂.

4.3 Heat Flux Distribution Estimation

Once the time independent distribution of T_G and α are obtained, the heat flux distribution during the spot heating tests can be estimated. In Fig. 4.10, is presented the calculated heat flux distribution over time for the preheating flame of 100% H₂. From the figure is observed the decrease in the heat flux over time and that the maximum distribution is located at R_0 .

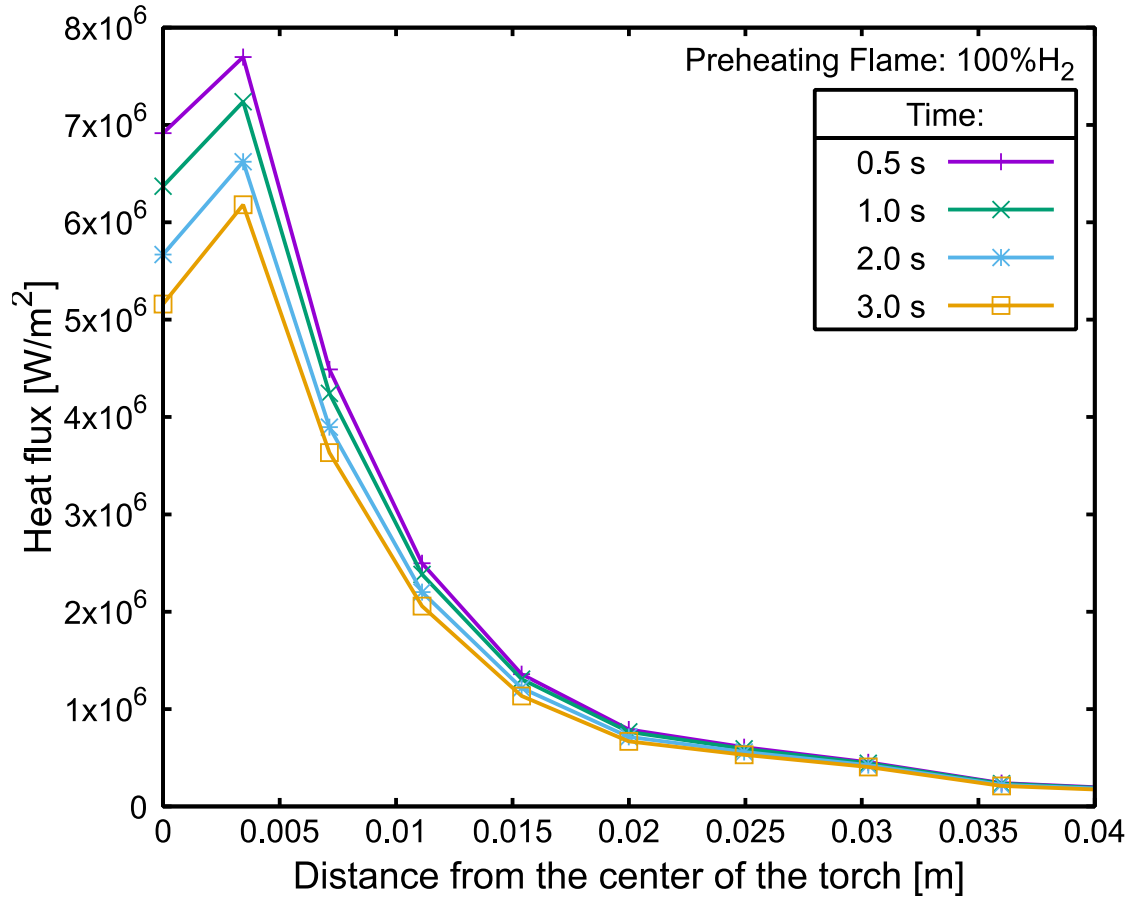


Fig. 4.10 Heat flux distribution over time when employing 100%H₂ as the preheating flame.

The comparison of the heat flux distribution for the chosen preheating flames are shown in Fig. 4.11. The figure show that the highest heat flux distribution is obtained for 100%H₂. Moreover, as the mixture rate of CO₂ and AR increases, the heat flux distribution decreases. In this regard CO₂, among all the evaluated preheating flames, shows the smallest heat flux distribution.

The obtained results show that the heat flux distribution becomes lower with the increase of the mixing ratio of the added gas. In addition, by comparing the reactive gas CO₂ with the non-reactive gas AR, it is considered that CO₂ has a harmful effect on the efficiency of the oxy-hydrogen cutting.

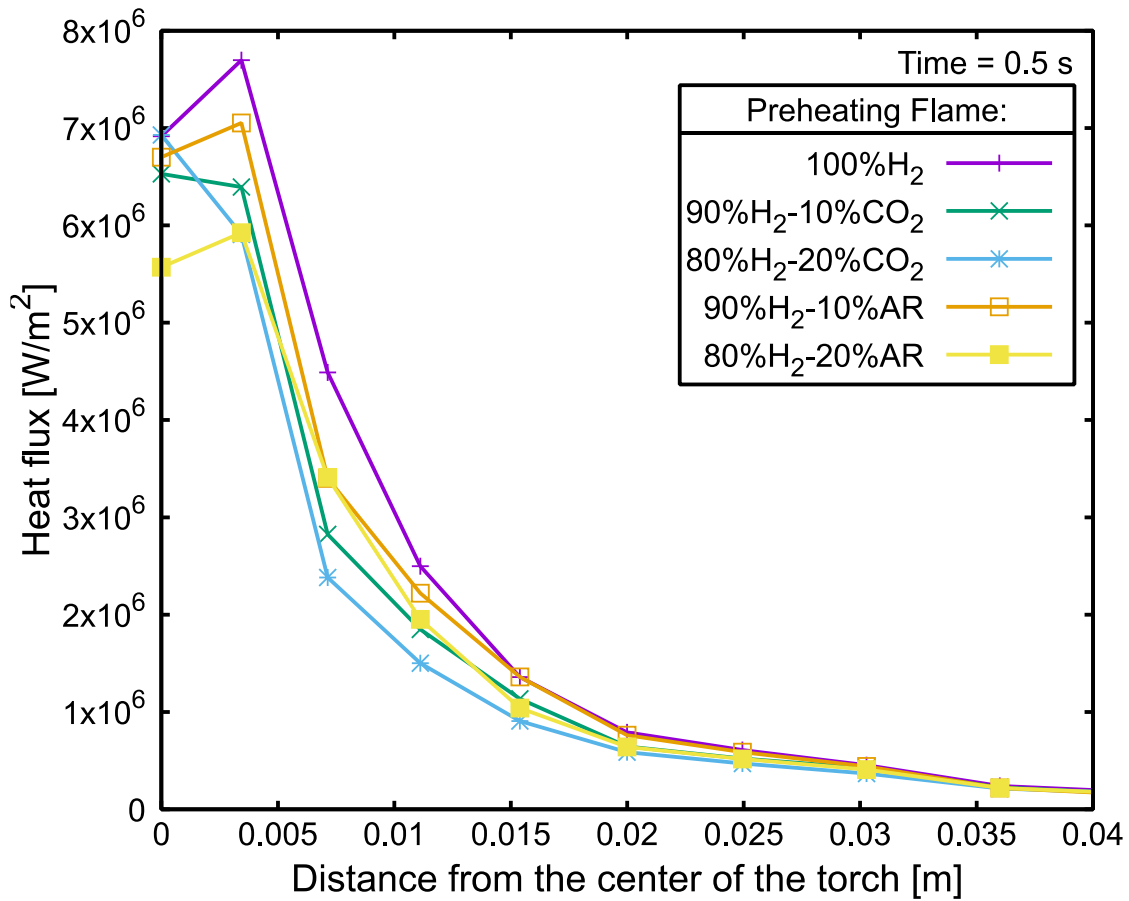


Fig. 4.11 Comparison of the heat flux distribution between the employed preheating flames.

4.4 Estimation of Piercing Performances

4.4.1 Model description

As reported by Osawa et al. (2012) by employing the identified heat transfer parameters T_G and α from the spot heating tests, it is possible to estimate the time until the plate surface temperature exceed the steels kindling temperature during the piercing tests by conducting a direct heat conduction analysis. The plate temperature during the preheating process is calculated by using the finite element code employed during the genetic algorithm analyses. The material properties and the calculation conditions are the same as those used in the inverse heat conduction analysis. The employed finite element model is an axisymmetric circular plate with a radius of 60 mm, and it comprises of 4 node iso-parametric quadrilateral elements. The element length ranges from 0.1mm to 6.95mm in radial direction and from 0.1mm to 2.02 mm in through thickness direction as shown in Fig. 4.12.

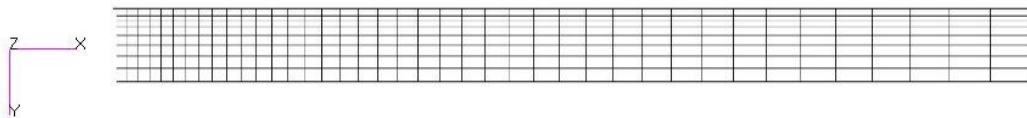


Fig. 4.12 Mesh employed for the direct heat conduction analysis of piercing tests.

4.4.2 Piercing time estimation

From the results of the piercing tests described in section 3.3, the employed preheating flame has a significant impact on the minimum piercing time required for the workpiece cutting. In order to check the accuracy of the identified heat transfer parameters, a numerical simulation of the piercing tests is performed. In this simulation, the newly identified heat transfer parameters are given to the model and the effect of the preheating flames is then evaluated.

Fig. 4.13 shows the calculated plate heating surface temperature at $r = 2, 3, 4, 5,$ and 6 mm during the piercing test preheated by $100\%H_2$. The figure shows the elapsed time from the beginning of the preheating. The heat surface temperature within the oxygen jet ($r < 4$ mm) exceeds the combustion point (1300 K) at 13 seconds. This condition leads us to the assumption that 1300 K is the temperature that triggers the metallic combustion.

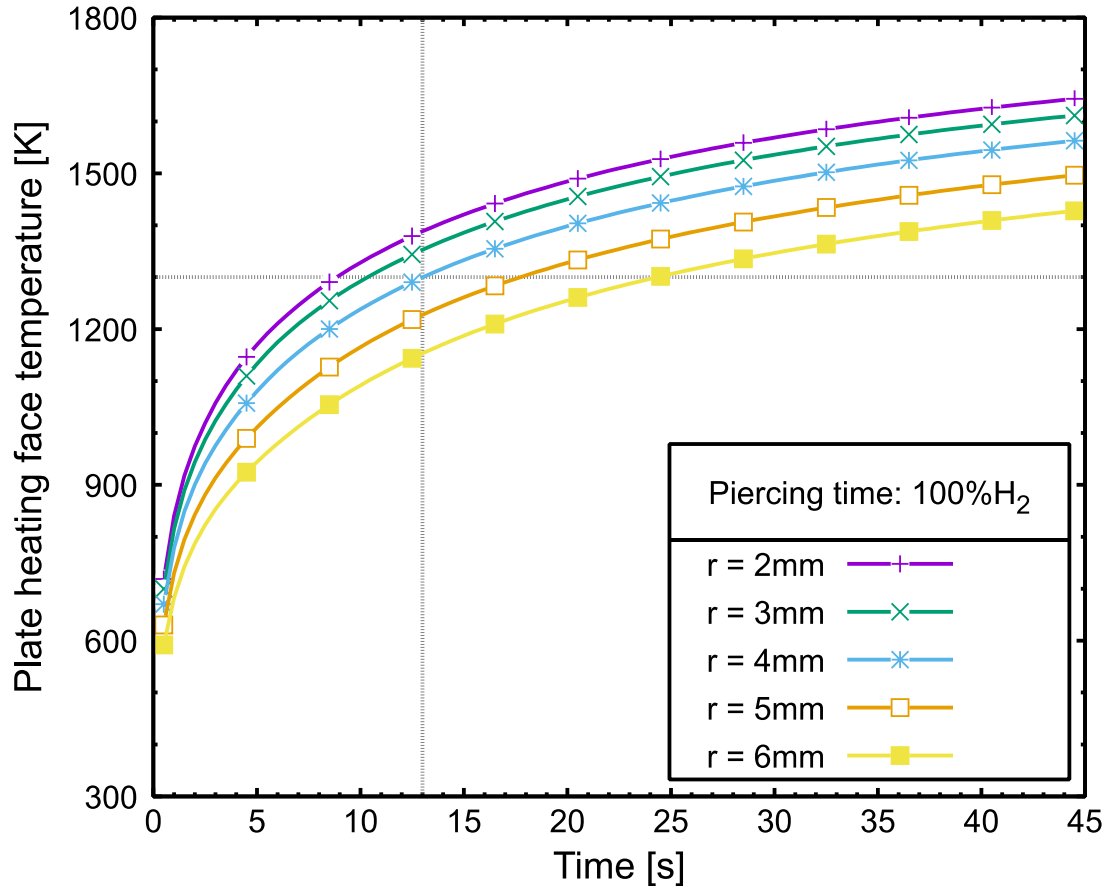


Fig. 4.13 Time histories of the heating face during piercing test at a distance ‘r’ from the center of the nozzle.

In a similar manner, the piercing simulation is conducted for the preheating flames 80% H₂-20% CO₂ and 90% H₂-10% AR. The comparison of the time histories of the plate surface temperature during the piercing test for the chosen preheating flames is shown in Fig. 4.14. By employing 1300K as the prerequisite for piercing, the minimum piercing time (t_{min}) is calculated. From the figure can be observed that the shortest t_{min} is obtained for 100% H₂ (13 secs). On the other hand, when

employing the preheating flames of CO₂ and AR, t_{min} is increased. For instance, by employing 90% H₂-10% AR t_{min} is increased by 12 secs (25 secs), while for 80% H₂-20% CO₂ t_{min} is increased by 40 secs (53 secs). The figure shows the negative impact when employing the preheating flames AR, and CO₂ in the oxy-hydrogen cutting performance.

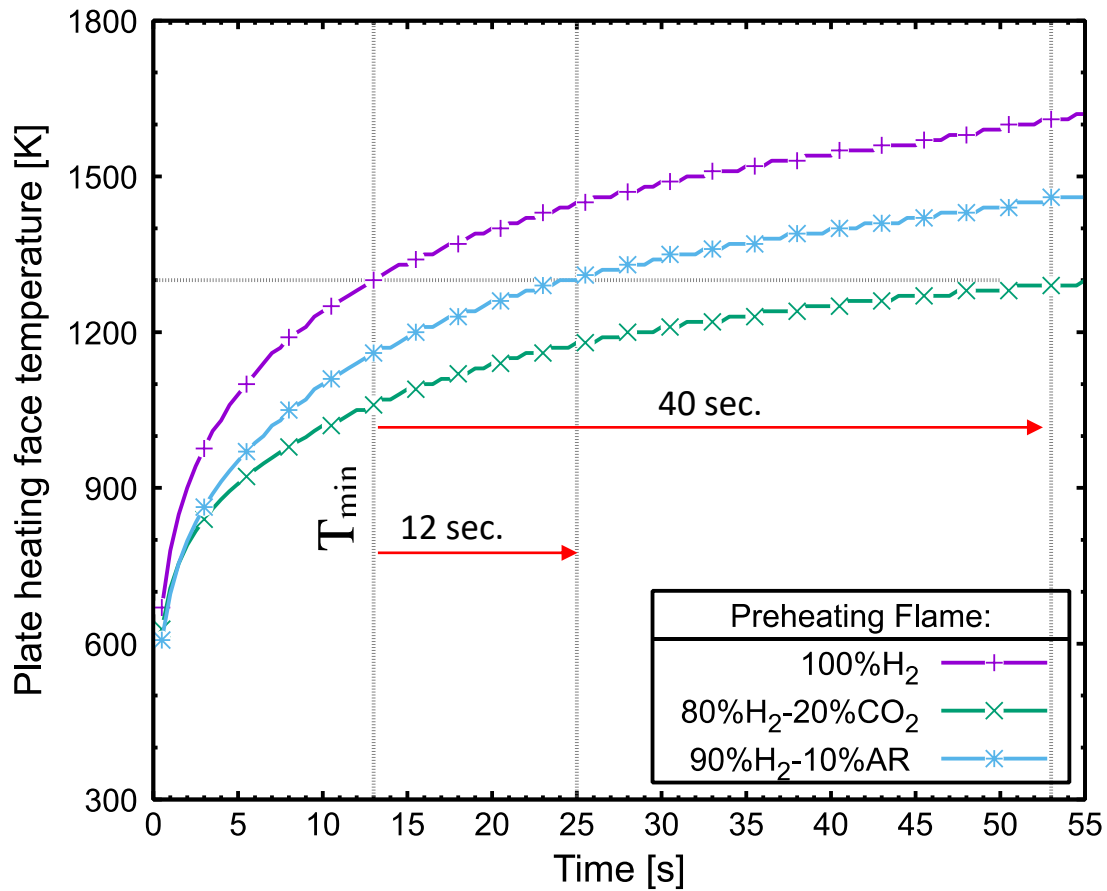


Fig. 4.14 Comparison of the time histories of plate surface temperature during piercing test for the different preheating flames.

Table 4.2 shows the comparison of the estimated t_{min} and the measured t_{min} during the piercing tests. The table shows that the simulated t_{min} shows good agreement with the experimental results. In this regard, the results show the effectiveness of the piercing process simulation as well as the accuracy of the identified heat transfer parameters.

Table 4.2 Estimated minimum piercing times

Preheating Flame	Estimated Minimum Piercing Time [sec]	Measured Minimum Piercing Time [sec]
100% H ₂	13	15
90% H ₂ - 10% AR	25	25
80% H ₂ - 20% CO ₂	53	50

4.5 Conclusions

In this chapter, the influence of the preheating flame composition on the oxy-hydrogen cutting performance is analyzed. The heat transfer parameters T_G and α are estimated following the heat conduction analysis method explained in Section 2.2. The accuracy of the estimated parameters is then evaluated by estimating the

backface temperature during the spot heating tests. Then, a numerical simulation of the piercing tests is performed. In this simulation, the newly identified heat transfer parameters are given to the model and the effect of the preheating flames on the oxy-hydrogen cutting is then evaluated. The following conclusions can be drawn from the obtained results.

- The reduction of the heat transfer coefficient for both the AR and CO₂ trials is almost same while the gas temperature of the AR mixture is similar to 100% H₂. However, for the CO₂ trials, not only the transfer coefficient but also the gas temperature declines.
- The heat flux distribution becomes lower with the increase of the mixing ratio of the added gas.
- By comparing the reactive gas CO₂ with the non-reactive gas AR, it is considered that CO₂ has a harmful effect on the efficiency of the oxy-hydrogen cutting.
- The comparison of the minimum piercing time shows the lower performance of the oxy-hydrogen cutting when employing CO₂ in the process.
- The results of the piercing time estimation show good agreement with the experimental results. The results show the effectiveness of the piercing process simulation and the accuracy of the identified heat transfer parameters.

Chapter 5

Numerical Simulation of the Gas Cutting Process

5.1 Introduction

Although the results of the piercing simulation show the harmful effect of the CO₂ in the oxy-hydrogen cutting, the deterioration mechanism has not been clarified. Based on the identified heat transfer parameters and the measured geometry from the gas cutting test, a three-dimensional simulation model is prepared in order to separately evaluate the preheating heat input and material combustion heat input. Challenges arise from the gas cutting test results, where inclined cutting-fronts was observed.

5.2 Gas Cutting Simulation

5.2.1 Implementation of the moving coordinate analysis

Osawa et al. [30] developed an in-house three-dimensional finite element code MOVEFLUX that can perform the quasi-stationary heat conduction analysis using a moving coordinate system (Section 2.3.2) and a local heat transfer model for preheating flame (Section 2.2). The heat transmitted to the workpiece from the preheating flame and the metallic combustion can be evaluated separately by using this code.

5.2.2 Model description

Based on the lower performance of the CO₂ during the piercing tests, the numerical simulation of the cutting process focuses on the preheating flames 100%H₂, and 80%H₂-20%CO₂ on the oxy-hydrogen cutting performance. Figs. 5.1 and 5.2. shows the heat transfer parameters employed during the analysis. The convective heat transfer coefficient between the workpiece and air is evaluated on the plate side and backface. Temperature-dependent material properties shown in Fig. 4.1 are used in analyses. The initial temperature is set to 300 K.

One-half finite element models shown in Figs. 5.3 and 5.4, are used during the finite element analyses. These models comprise 8 node isoparametric hexagonal elements. As shown in Table 3.4, it was observed that there was no significant

difference in the in-plane groove's edge shape between 100% H_2 -0% CO_2 and 80% H_2 -20% CO_2 . The groove's leading edge can be approximated by a semicircle with radius a ($d/2$) of 1.5 mm. Therefore, the same in-plane one-half mesh is adopted for both cases, the three-dimensional meshes are generated by extruding this in-plane mesh. For this in-plane mesh, fine quadrature elements are arranged along the curved groove edge, and they are configured so that the mesh becomes sparser as the distance from F (Fig. 2.3) increases. The minimum element edge length is 0.236 mm along the edge, and 0.243 mm in the normal direction of the edge.

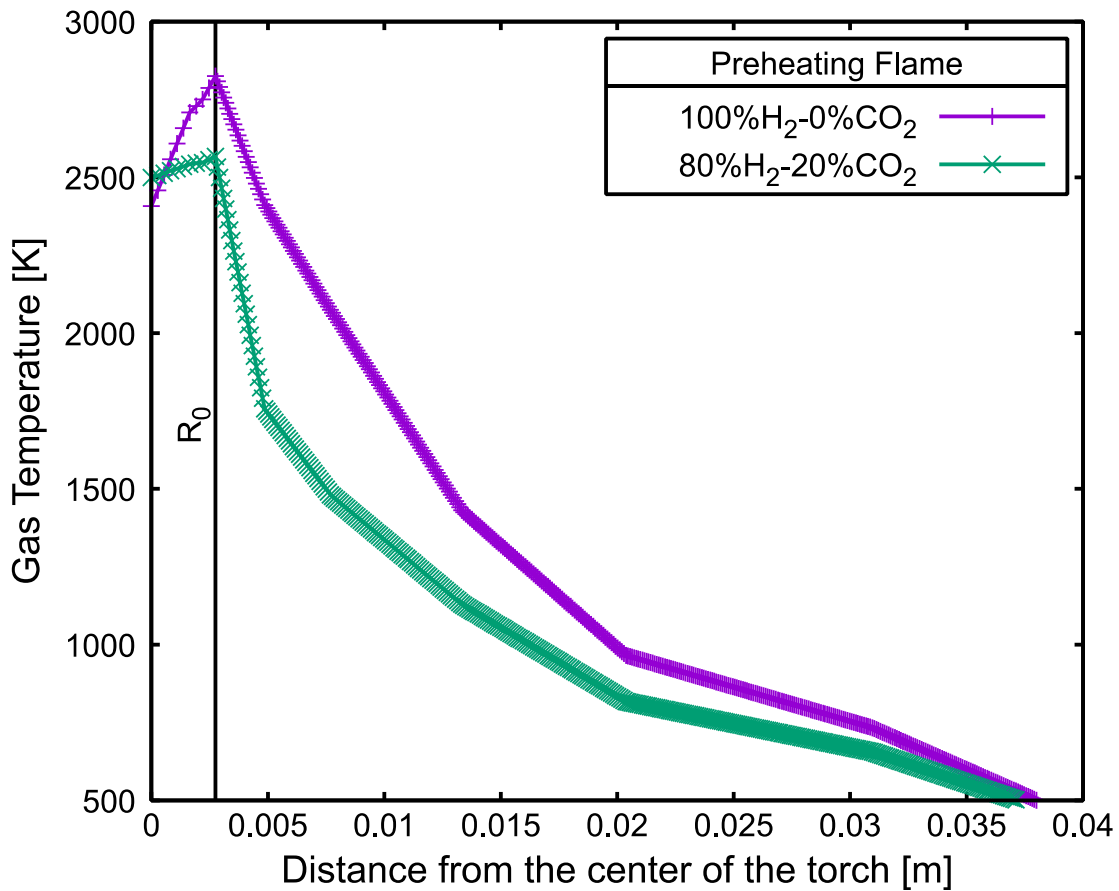


Fig. 5.1 Identified gas temperature distribution.

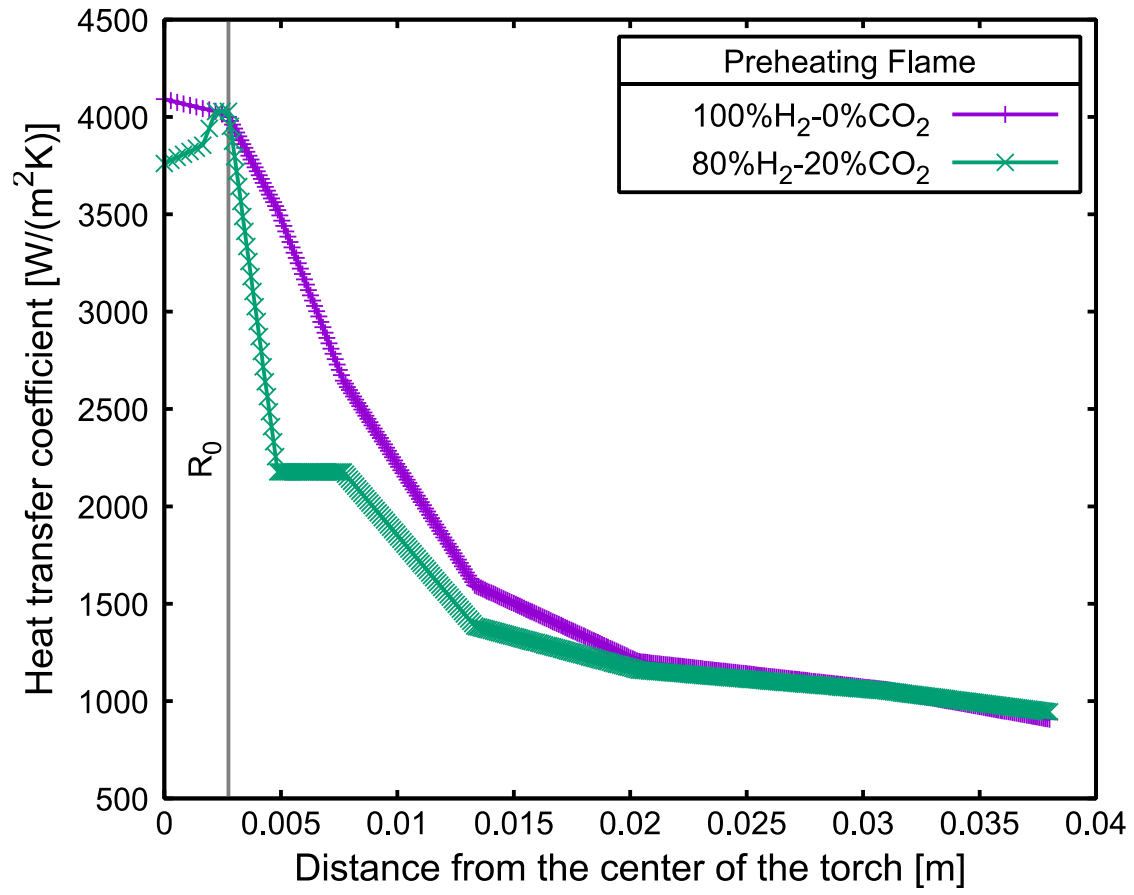
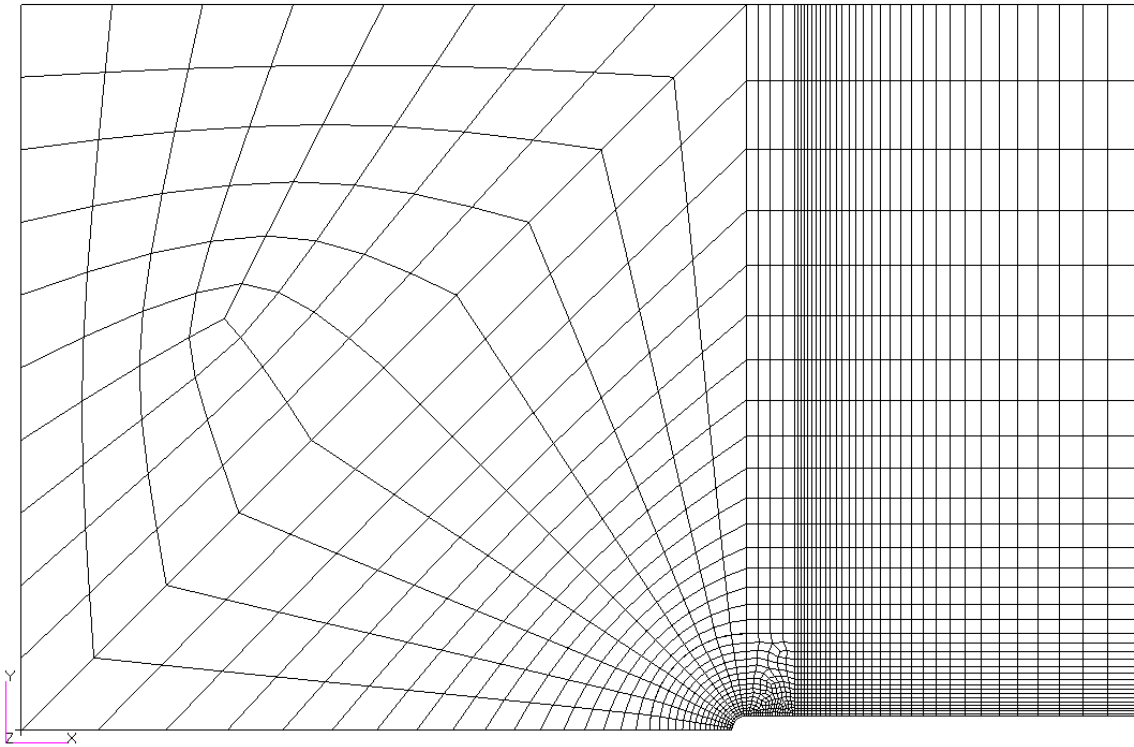


Fig. 5.2 Identified heat transfer coefficient distribution.

(a)



(b)

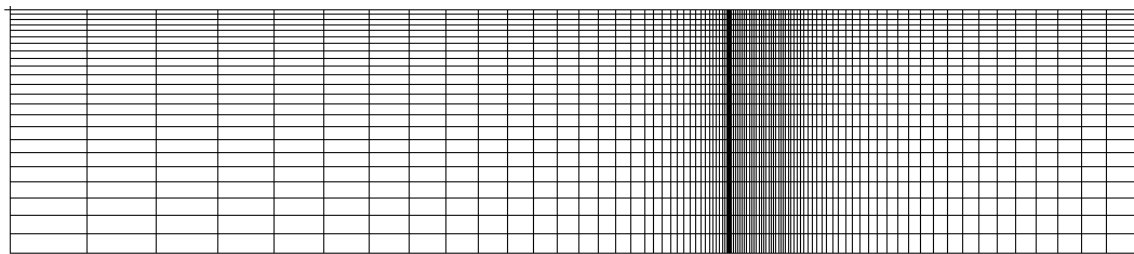
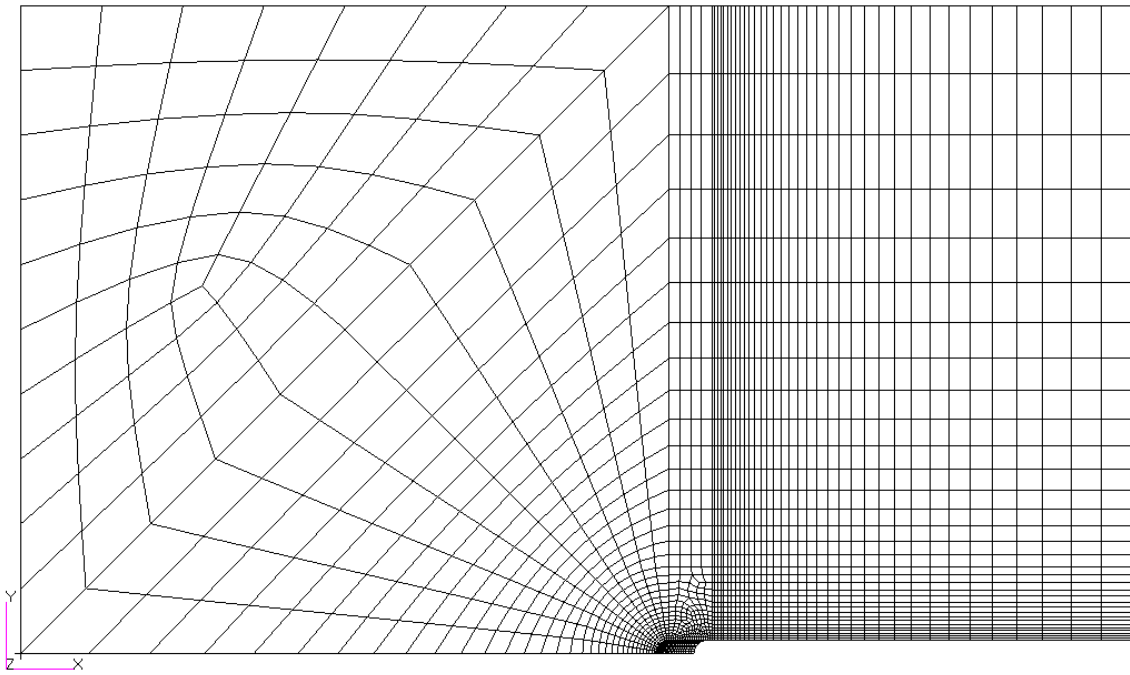
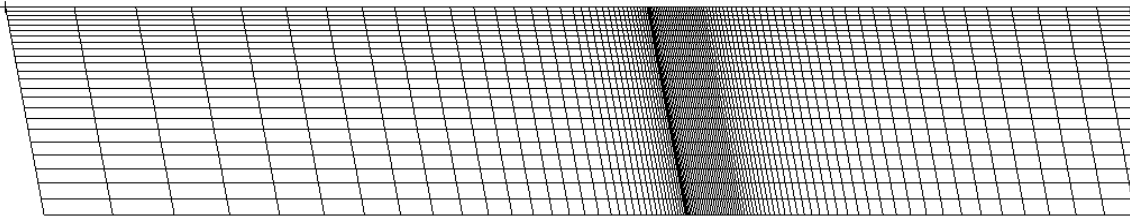


Fig. 5.3 Finite element mesh used for 100% H_2 -0% CO_2 heat conduction analysis. (a) top view (b) side view.

(a)



(b)



(c)

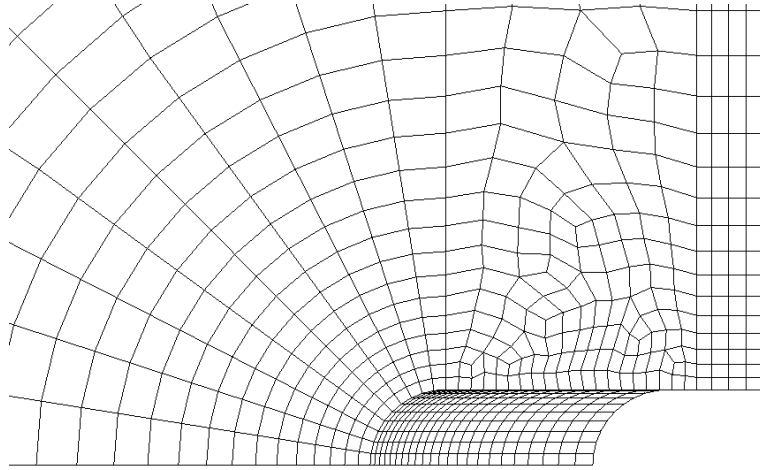


Fig. 5.4 Finite element mesh used for 80% H_2 -20% CO_2 heat conduction analysis. (a) top view. (b) side view. (c) enlarged view of the cutting groove.

Table 3.4 shows that the cutting front drag κ was negligible for 100% H_2 -0% CO_2 while it was about 14 % of the plate thickness (25 mm) for 80% H_2 -20% CO_2 . Therefore, the extrusion is performed along the normal direction for 100% H_2 -0% CO_2 , and along the inclined direction for 80% H_2 -20% CO_2 (Figs. 5.3 and 5.4). The element size is configured so that the edge length in thickness direction becomes larger with the distance from the front face. The minimum edge length in the thickness direction is 0.5 mm. The total number of nodes and elements are 67536 and 61893 respectively. Because of the inclined extrusion direction, the model end shows inclined cross section for 80% H_2 -20% CO_2 . However, this does not affect the

accuracy of the temperature calculation because the uniform room temperature is given to the nodes on this section, during the time integration of the heat conduction analysis when the temperature is updated.

5.2.3 Kerf temperature estimation

Provisional kerf temperature calculation

Once groove's geometry ($a=d/2$ and λ) and torch speed V are given, $T_{2D}(s)$ in Section 3.5.3 can be calculated by Matsuyama's method [37] as

$$\tilde{T}_I = \exp(-\mu_I \cos(\phi_I)) \sum_{n=0}^{N-1} C_n K_n \cos((I-1)\phi_I); \tilde{T}_I = T/T_f \quad (5.1)$$

Where,

$$\{C_n\} = ([A_{In}]^T [A_{In}])^{-1} [A_{In}]^T \{B_I\}$$

A_{In}

$$= \begin{cases} \exp(-\mu_I \cos \phi_I) K_n(\mu_I) \cos(n\phi_I) & (1 \leq I \leq L) \\ K_n(\mu_I) \left[-\cos\left(\frac{\pi}{2}\right) \cos(n\phi_I) - \frac{1}{v} n \sin\left(\frac{\pi}{2} - \phi_I\right) \right] & (L+1 \leq I \leq L+M) \end{cases} \quad (5.2)$$

$$B_I = \begin{cases} 1.0 & (1 \leq I \leq L) \\ 0.0 & (L+1 \leq I \leq L+M) \end{cases}$$

In Eqs. (5.1) and (5.2), K_n is the modified Bessel function of the n-th order, I the collocation point number, T_f the melting point, $\mu_i = Vr_i/2k$, k is the thermal

conductivity, r and ϕ are defined in Fig. 2.3, L and M, numbers of collocation points in S1 and S2 boundaries. In the same manner as Osawa et al. [30], parameters shown below are adopted.

1. The groove leading edge is approximated as semicircle with $a = 1.5$ mm and $y = \phi$. T_f is set to 1800 K [43].
2. The S_1 boundary starts at point F (Fig. 2.3) and ends at the point right beside the torch center (point M in Fig. 2.3). The length of S_2 and S_3 boundaries l_1 and l_2 , are $0.5a$ and $1.1a$. l_1 is altered in the following iterative analyses.
3. S_1 is divided into 15 equal sections, S_2 into 7 equal sections and S_3 into 15 equal sections and the collocation points are arranged at the section division points.

The calculated T_{2D} along the solidification line is shown in Fig. 5.5, This temperature distribution is given to the finite element nodes on the kerf as the provisional temperatures for the three-dimensional analyses.

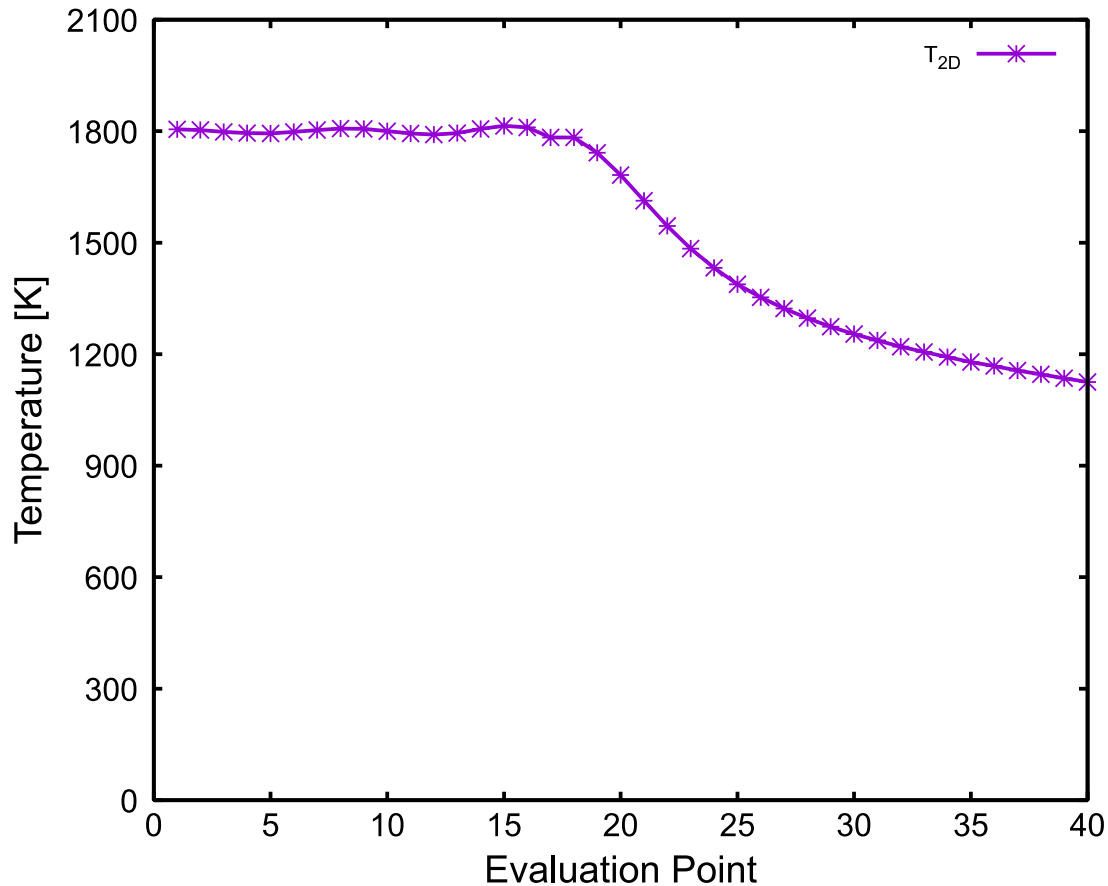


Fig. 5.5 Change of the kerf temperature along the solidification line.

Three-dimensional kerf temperature distribution

The three-dimensional temperature distribution on the cutting groove is calculated by MOVEFLUX adopting the provisional two-dimensional kerf temperature (T_{2D}) to each evaluation plane. This result is called ‘provisional solution’. For 100% H_2 -0% CO_2 model, the provisional solution’s three-dimensional quasi-stationary temperature field is shown in Fig. 5.6, and the kerf temperature distribution on the heating face is shown in Fig. 5.7. As expected in Section 2.3.6, a

sharp temperature discontinuity is observed in the vicinity of the S_2/S_3 border. Fig. 5.7 shows that T_{3D} on the S_3 boundary is higher than T_{2D} . This is due to the heat supply from the preheating flame (Osawa et al. [30]).

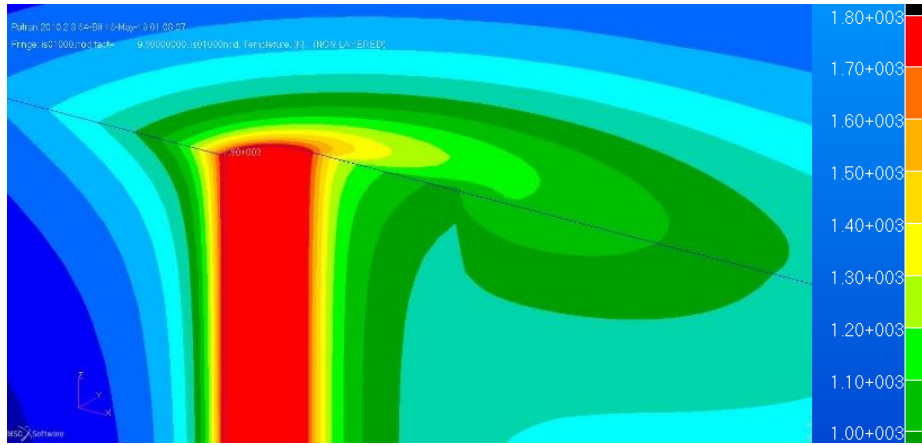


Fig. 5.6 Temperature discontinuities generated during the 100% H_2 -0% CO_2 three-dimensional heat conduction analysis.

As discussed in Section 2.3.6, this discontinuity can be overcome by adjusting the length of S_2 boundary l_1 on each evaluation plane $\pi(z)$. S_2 temperature near the S_2/S_3 border can be raised by increasing l_1 , while it can be decreased by reducing l_1 . This adjustment is performed iteratively so that T_{3D} becomes close to T_{2D} at the border on every $\pi(z)$, by repeating the process, a smooth and continuous temperature distribution along both the solidification line and the thickness direction is achieved.

For the 100% H_2 -0% CO_2 model, the temperature field without discontinuity and the smooth kerf temperature distribution along the solidification line and the thickness direction, which are derived from the adjusted kerf temperature on each plane, are shown in Figs. 5.8 and 5.9. These results demonstrate the kerf temperature adjustment technique proposed in Section 2.3.6, is effective to the thicker plate (25 mm-thick) considering non-inclined straight leading edge. Fig. 5.10 shows the calculated heating face temperature distribution for 100% H_2 -0% CO_2 at $V=5$ mm/sec. by implementing the proposed technique. The result shows the smooth and continuous temperature distribution in the heating face during the analysis.

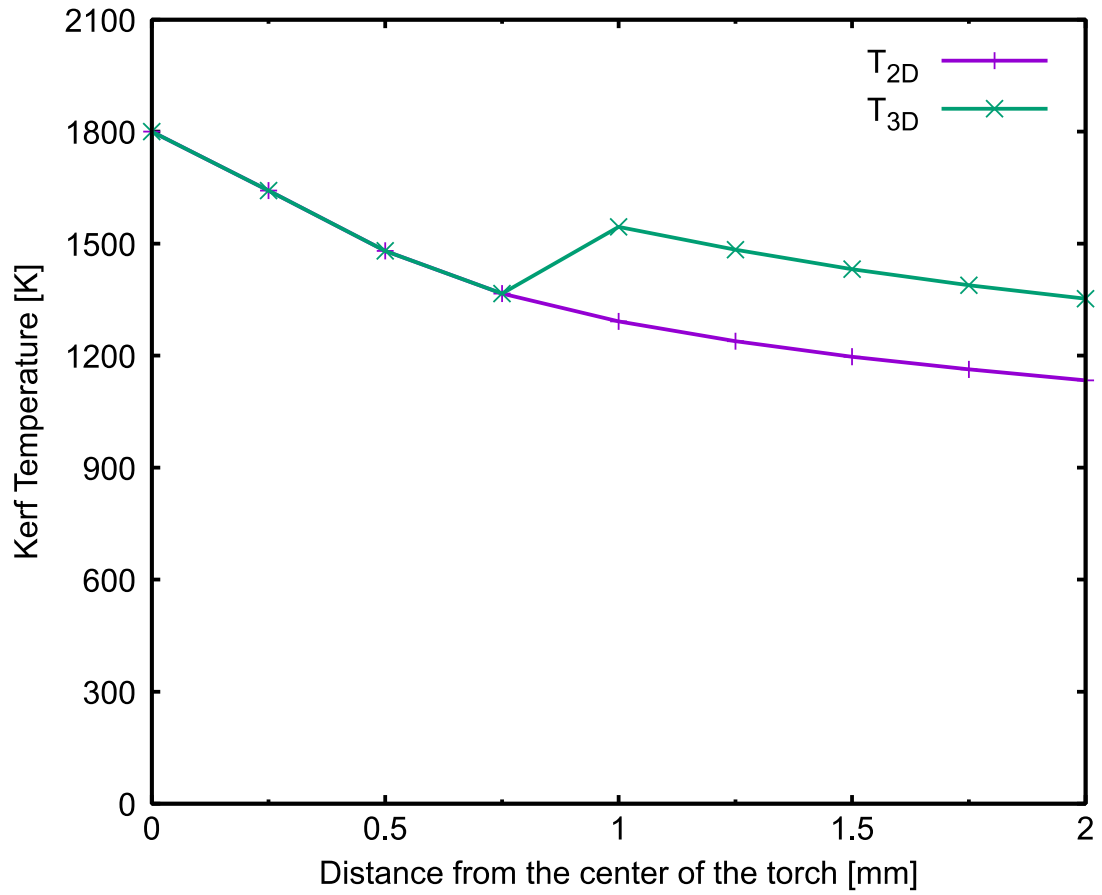


Fig. 5.7 Comparison of kerf temperature on the heating face obtained by Matsuyama's two-dimensional solution and that from the three-dimensional analyses.

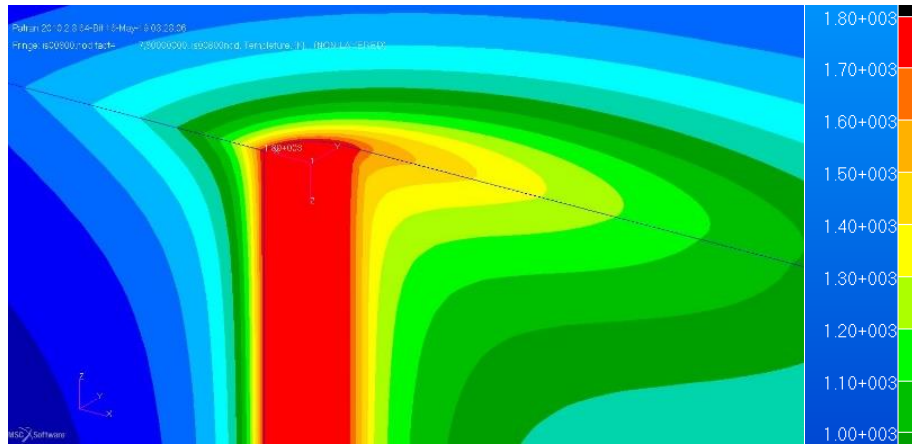
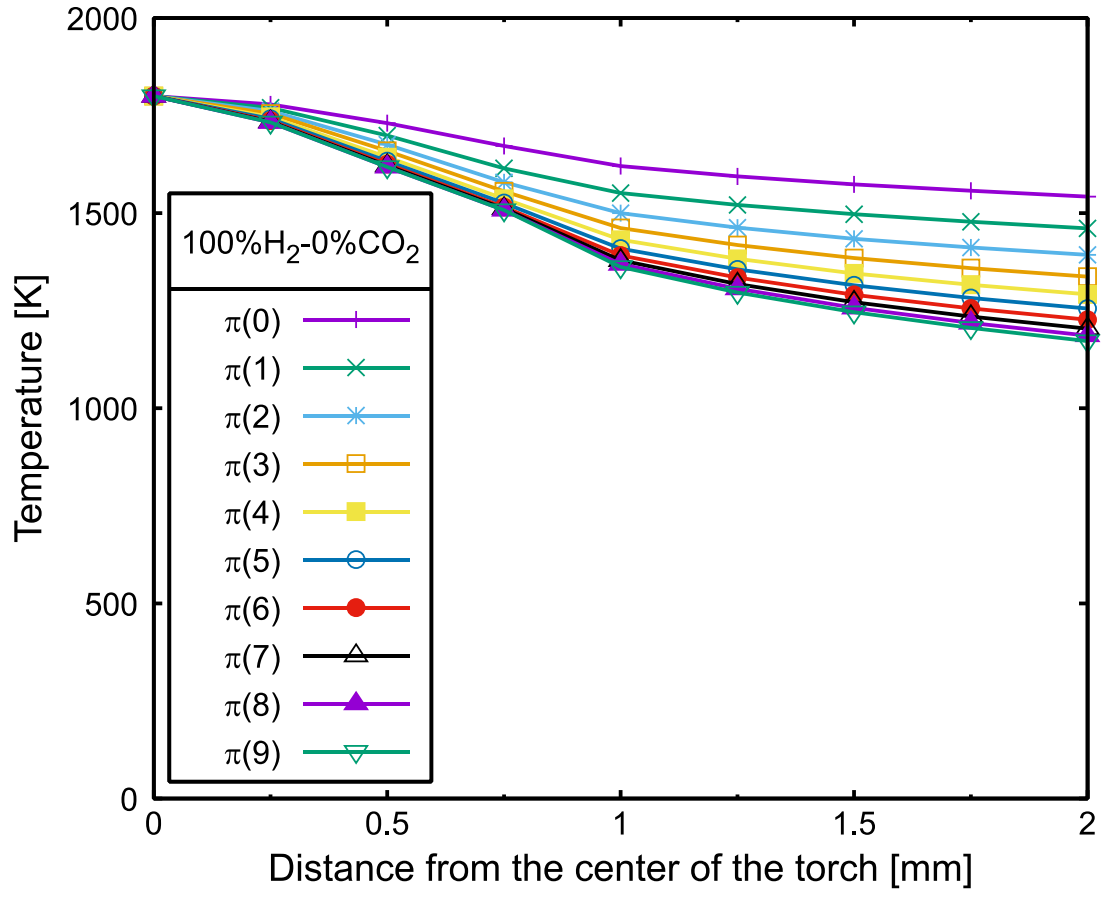


Fig. 5.8 Three-dimensional quasi-stationary temperature field without discontinuity obtained from the adjusted two-dimensional kerf temperature on each evaluation plane (case 100% H₂-0% CO₂).

(a)



(b)

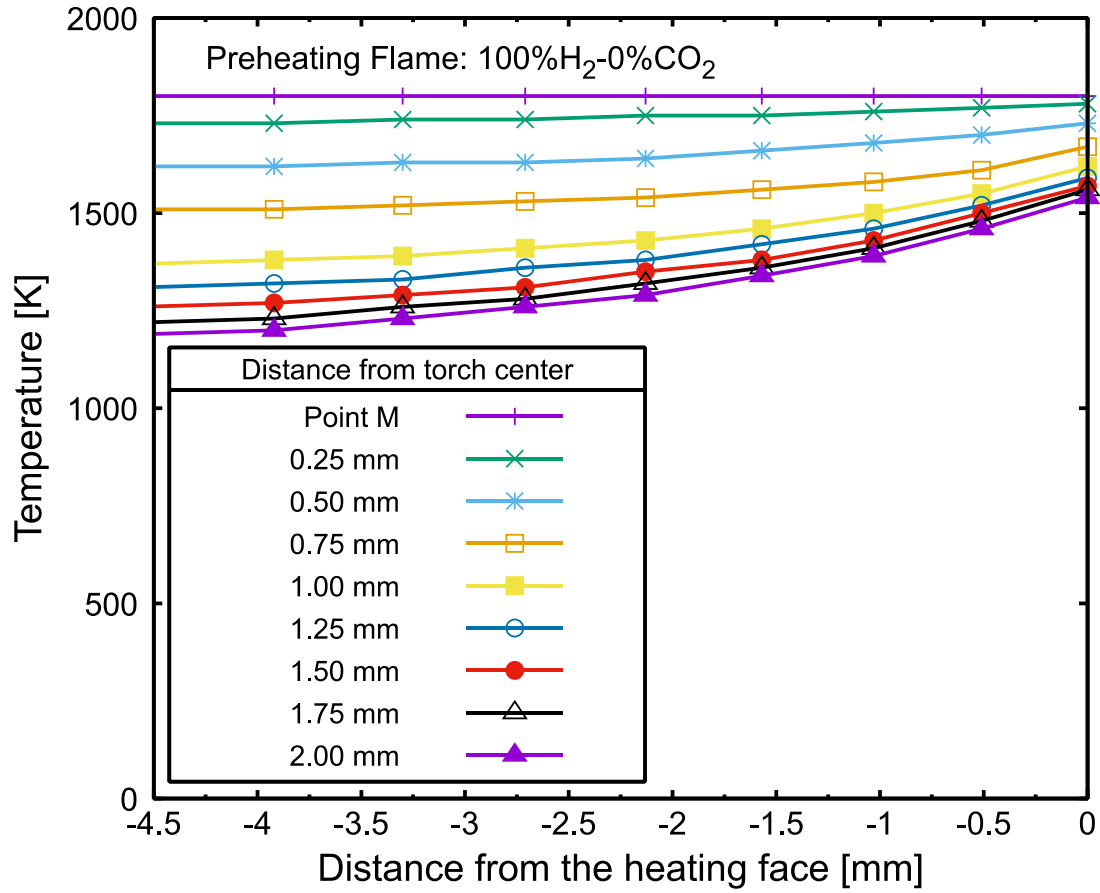


Fig. 5.9 Kerf temperature distribution obtained from the adjusted groove temperatures. (a) along the solidification line on each evaluation plane. (b) along the thickness direction (case 100%H₂-0%CO₂).

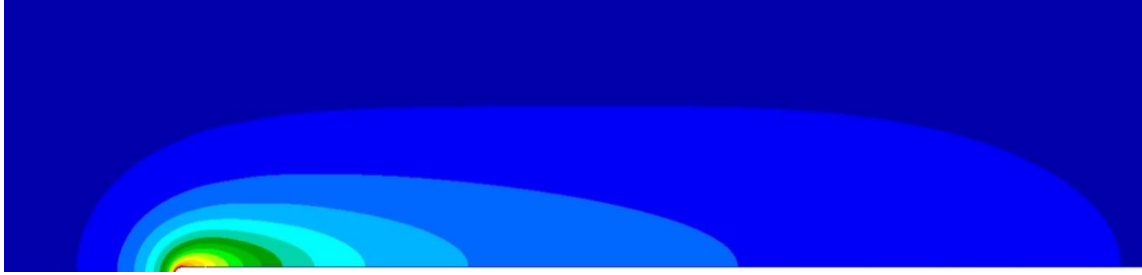


Fig. 5.10 Calculated heating face temperature for 100% H_2 -0% CO_2 .

The proposed kerf temperature adjustment technique is applied to the 80% H_2 -20% CO_2 model, which shows an inclined cutting-front. The adjusted temperature field without discontinuity is shown in Fig. 5.11, and the smooth groove temperature distribution along the solidification line and the thickness direction are shown in Fig. 5.12. In the same manner as 100% H_2 -0% CO_2 case, smooth and continuous temperature distribution along both the solidification line and the thickness direction are achieved. This means that the proposed technique can be applied to thicker plates with inclined cutting-front.

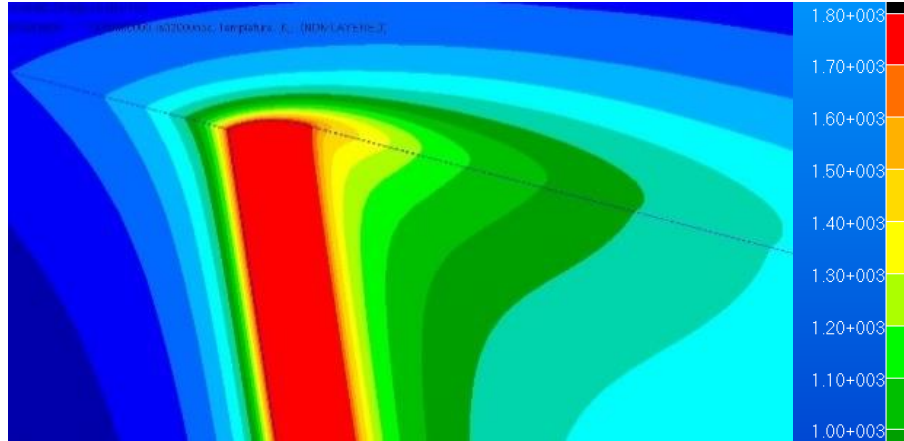
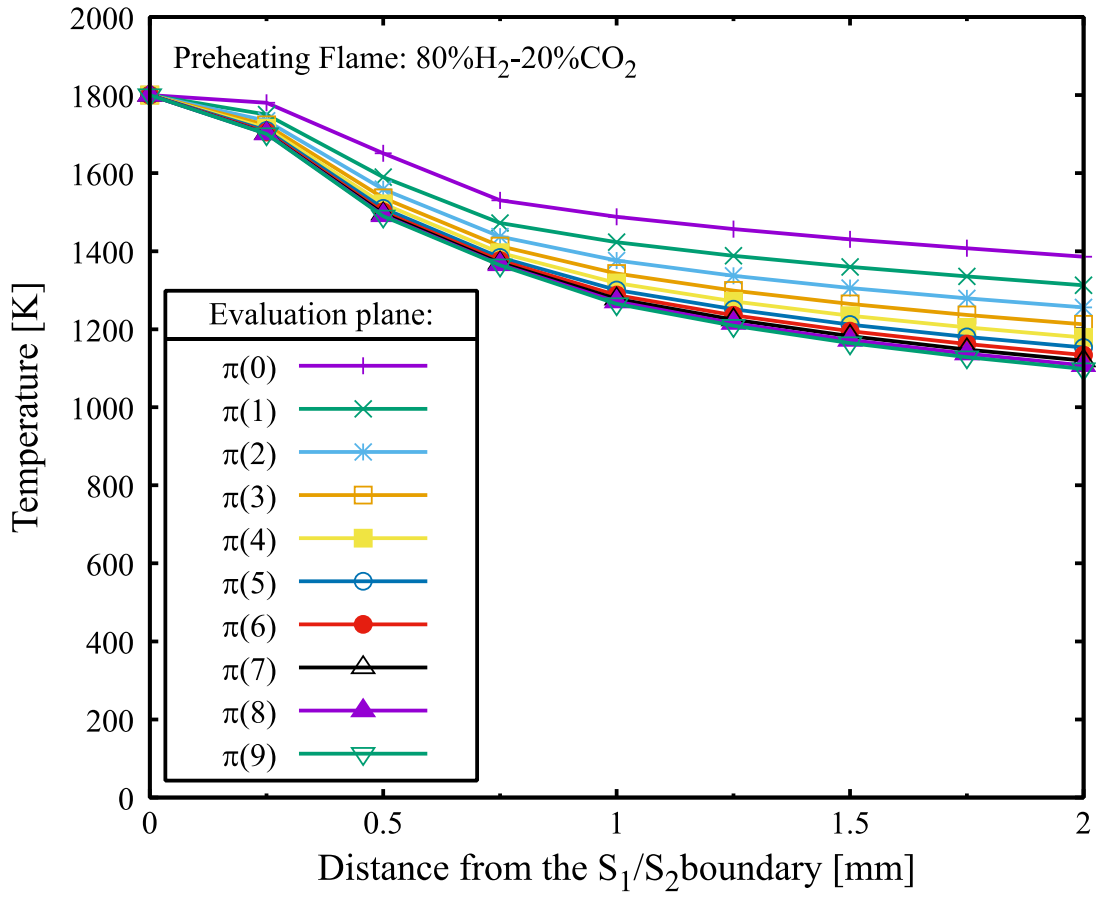


Fig. 5.11 The three-dimensional quasi-stationary temperature field without discontinuity obtained from the adjusted two-dimensional kerf temperature on each evaluation plane (case 80% H_2 -20% CO_2).

(a)



(b)

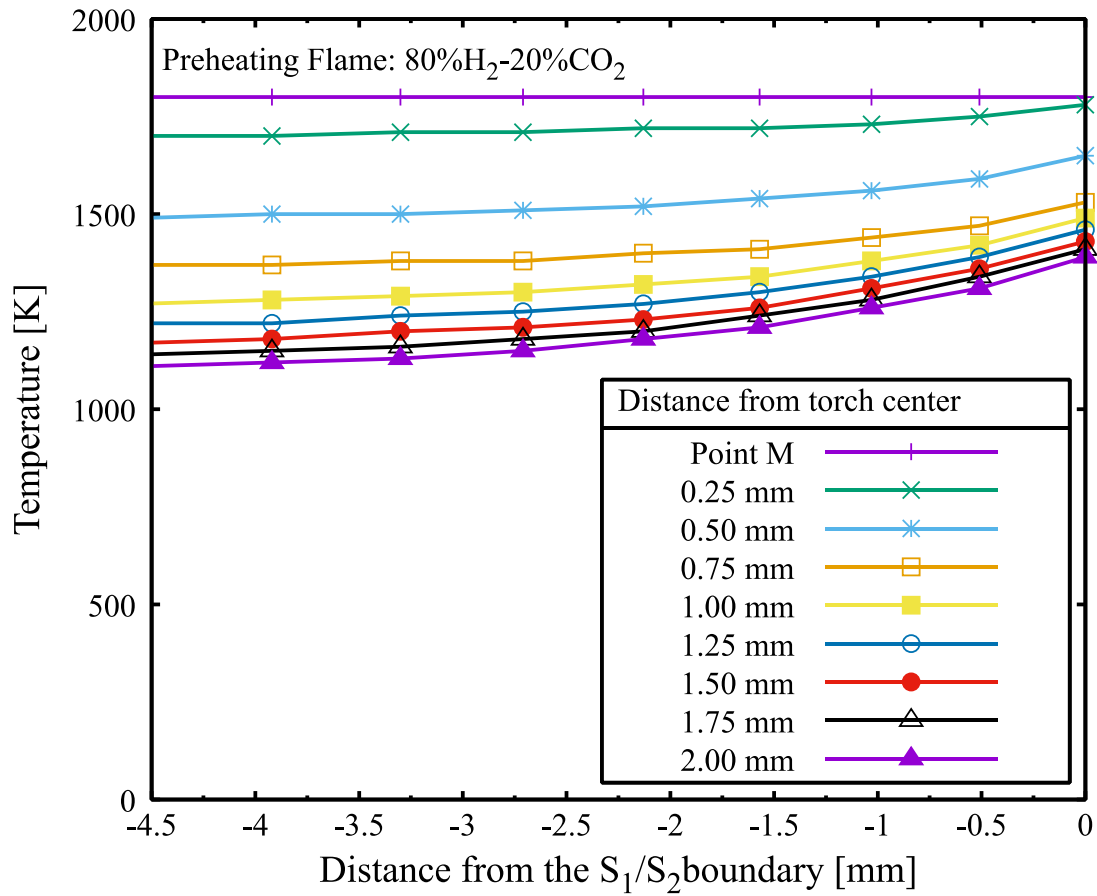


Fig. 5.12 Kerf temperature distribution obtained from the adjusted groove temperature. (a) along the solidification line on each evaluation plane (b) along the thickness direction (case 80%H₂-20%CO₂).

5.3 Cutting Performance Analysis

The heat input from preheating gas, q_G can be calculated by integrating the heat flux due to preheating heat transfer. The heat flux on the kerf can be estimated from the temperature gradient in the element adjacent to the kerf. The heat input due to

material combustion (self-burning), q_B , is calculated by integrating heat flux on the kerf. Let q_{total} be the sum of q_G and q_B . Heat inputs per unit time are calculated.

Table 5.1 and Fig. 5.13 shows calculated q_G , q_B , and q_{total} for the preheating flames 100% H_2 -0% CO_2 and 80% H_2 -20% CO_2 . The table and figure show that q_G per unit time of 100% H_2 -0% CO_2 is about 43% larger than that of 80% H_2 -20% CO_2 , while the difference in q_B is small (about 0.97%)

Table 5.1 Heat flux per unit time.

Preheating gas	Cutting speed [mm/s]	Heat flux per unit time		Total [J/s]
		q_G	q_B	
100% H_2 - 0% CO_2	5	2299	2542	4841
80% H_2 - 20% CO_2	5	1606	2567	4173

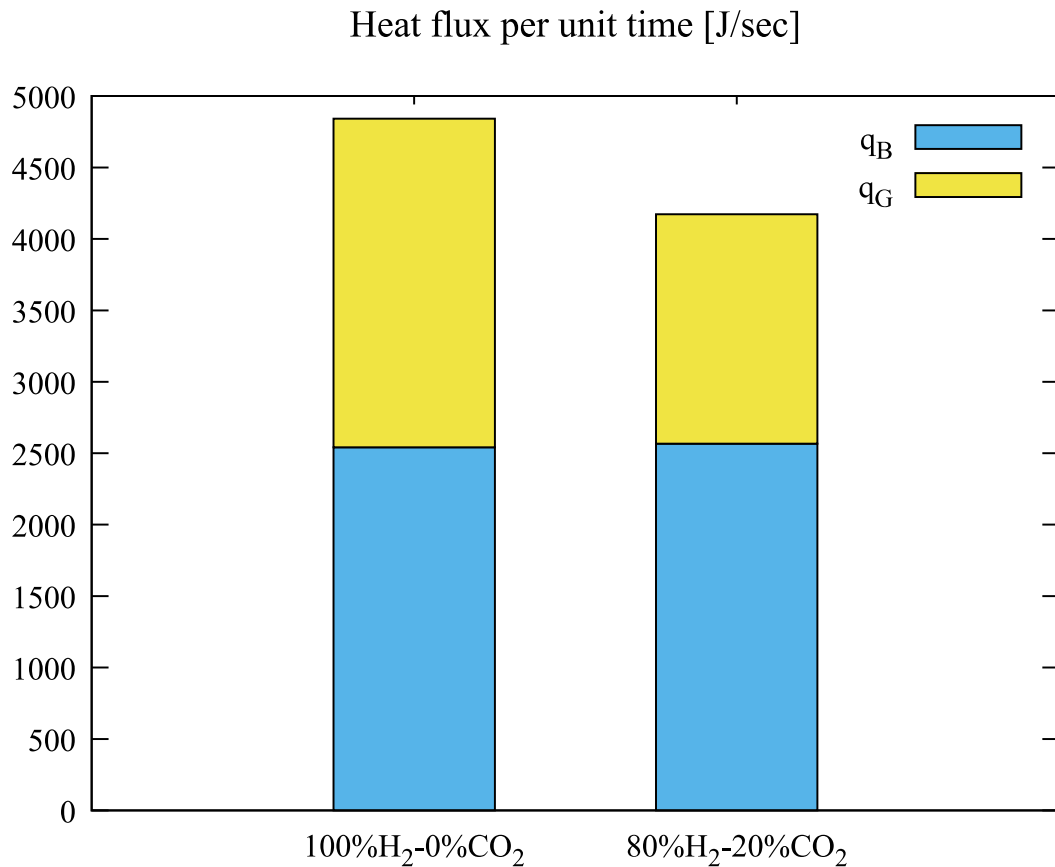


Fig. 5.13 Heat input from the preheating gas flame and that from the material combustion.

Table 5.1 shows that the amount of the burning gas (H_2) and oxidizing agent (O_2) supplied in the 80% H_2 -20% CO_2 preheating flame is the same as that for the 100% H_2 -0% CO_2 preheating flame. The results of Table 5.1 and Fig. 5.13 show that the heat transfer from the preheating flame significantly decreases when CO_2 is mixed into H_2 , while the heat efficiency of material combustion is hardly affected by the presence of CO_2 when the same amount of Oxygen is supplied.

Ikegami [31] reported that the cutting performance of Oxy-Hydrogen cutting deteriorates when CO₂ is mixed into the preheating gas, and he supposed that this deterioration was due to the decline in the heat efficiency of material combustion. However, the results obtained in this study suggest that the cutting performance deterioration by the presence of CO₂ observed in Ikegami's experiment was caused solely by the decrease in the heat transfer from the preheating flame.

5.4 Conclusions

A new procedure for the kerf temperature estimation throughout the plate thickness based on the two-dimensional analysis of Matsuyama et al. [37] is established. The procedure allows a smooth and continuous temperature distribution through the plate thickness direction by the iterative adjustment of the S₂ boundary length on each evaluation plane.

By applying the proposed procedure, it is possible to estimate the three-dimensional kerf temperature distribution on thick plates and also allows the consideration of inclined cutting fronts during the analysis.

By evaluating the preheating, and the material combustion heat input, it is observed a substantial decline in q_G while employing 80% H₂-20% CO₂ preheating flame whereas, q_B remains unchanged regardless of the employed preheating flame.

The results obtained in this study suggest that the cutting performance deterioration reported by Ikegami [31] was caused solely by the decrease in the heat transfer from the preheating flame.

Chapter 6

Conclusions and Recommendations

6.1 Introduction

This chapter summarized the thesis and identifies the major contribution by this research study. Directions for future work and possible extensions to this research are presented at the end of this chapter.

6.2 Conclusions and Contributions

In this research, the influence of the CO_2 on the oxy-hydrogen cutting performance is studied in terms of the CO_2 content on the preheating flame and the heat transfer role of the CO_2 during the cutting process. To study the influence of CO_2 content on the preheating flame a numerical simulation of the piercing process is carried out and validated with an experiment piercing process test. On the other hand, to study the heat transfer role of CO_2 , a simulation of the oxy-hydrogen cutting

process is carried out and the results are compared with the results from the literature.

The conclusions of the present study can be summarized as follows,

(1) The theories and methods incorporated in the computational analyses throughout this study are introduced. During this research, heat transfer parameters of the preheating flames are identified by a genetic algorithm analysis developed by Osawa et al. [12]. A three-dimensional gas cutting simulation for the quantitative evaluation of the heat transfer based on the code previously developed by Osawa et al. [30] is implemented. A new technique for the analysis of inclined cutting-fronts during the oxy-hydrogen cutting simulation is proposed.

(2) To quantify the effects of the preheating flame characteristics on the cutting performance a series of experiments were carried out during this study, the obtained results can be summarized as follow,

- a. From the spot heating test, experiment show that as the mixing ratio of the added gas (AR, CO₂) increases, the measured temperature at the back-face of the plate decreases. Moreover, by comparing the employed added gas (AR & CO₂), the measured temperature at the back-face of AR trials were higher than CO₂ trials.

- b. From the piercing test, the experiments show a clear deterioration in the cutting performance when employing 80% H_2 -20% CO_2 , the minimum piercing time t_{min} was increased by 40 secs.
- c. From the gas cutting test, the experiments show a clear deterioration in the quality of the cut when employing 80% H_2 -20% CO_2 .

(3) To study the influence of the preheating flame state on the cutting performance, the heat transfer parameters T_G and α are identified and then validated with the results of the piercing tests. The obtained results can be summarized as follows,

- a. The reduction of the heat transfer coefficient for both the AR and CO_2 trials is almost same while the gas temperature of the AR mixture is similar to 100% H_2 . However, for the CO_2 trials, not only the transfer coefficient but also the gas temperature declines.
- b. The heat flux distribution becomes lower with the increase of the mixing ratio of the added gas.
- c. By comparing the reactive gas CO_2 with the non-reactive gas AR, it is considered that CO_2 has a harmful effect on the efficiency of the oxy-hydrogen cutting.

- d. The comparison of the minimum piercing time shows the lower performance of the oxy-hydrogen cutting when employing CO₂ in the process.
- e. The results of the numerical piercing time estimation show good agreement with the measured piercing times. The results show the effectiveness of the piercing process simulation and the accuracy of the identified heat transfer parameters.

(4) The ratio of the preheating heat input and the material combustion heat input is examined by performing a three-dimensional simulation of the oxy-hydrogen cutting process. The results of the proposed technique for the analysis of inclined cutting-fronts is examined. Based on the simulation results, CO₂ deterioration mechanism on the oxy-hydrogen cutting performance is then discussed. The obtained results can be summarized as follows,

- a. A new procedure for the kerf temperature estimation throughout the plate thickness based on Matsuyama et al.'s [37] method is established. The procedure allows a smooth and continuous temperature distribution through the plate thickness direction by the iterative adjustment of the S₂ boundary length on each evaluation plane.

- b. By applying the proposed procedure, it is possible to estimate the three-dimensional kerf temperature distribution on thick plates and also allows the consideration of inclined cutting fronts during the analysis.
- c. By evaluating the preheating, and the material combustion heat input, it is obtained a substantial declined in q_G while employing 80% H_2 -20% CO_2 preheating flame whereas, q_B remains unchanged regardless of the employed preheating flame. The results obtained in this study suggest that the cutting performance deterioration reported by Ikegami [31] was caused solely by the decrease in the heat transfer from the preheating flame.

6.3 Recommendations

As the future research, the following issues need to be investigated.

- The present study focuses on the influence of CO_2 on the oxy-hydrogen cutting performance. Further validation of the proposed technique through the comparison with different preheating flames should be carried out.
- During the gas cutting simulation a constant cutting front angle were used during the analyses. It is highly desirable to study the effects of the cutting front angle throughout the thickness direction during the analysis.

- During this study, the influence of CO₂ in the cutting performance was evaluated employing a cutting speed of 5 mm/s, further validation of the proposed technique through the comparison with different cutting speeds should be carried out.
- Now that a numerical method to evaluate the heat input ratio during the oxy-hydrogen cutting process has been established, data bases of common preheating flames can be generated and the preheating flame optimization could be carried out automatically by implementing algorithms to select the best preheating flame composition.

References

- [1] M. T. Ramaswamy, Heat Affected Zone Studies of Thermally Cut Structural Steels, OHSU Digital Collections, 1989.
- [2] L. Jeffus, Welding: Principles and Applications, Cengage Learning, 1997.
- [3] K. Weman, Welding Processes Handbook, Woodhead Publishing, 2012.
- [4] Welding Handbook 9th Edition, American Welding Society, 2001.
- [5] S. W. Miller, Oxy-acetylene Welding, The Industrial Press, 1916.
- [6] The Oxy-Acetylene Handbook, Union Carbide Carbon Corp, 2000.
- [7] Bruce, G., Eyres, D., Ship Construction 7th Edition, Butterworth Heinemann, 2012.
- [8] Munoz-Escalona, P., Payares, M.C., Dorta, M., Dias, R., "Analysis and Influence of Acetylene and Propane Gas During Oxyfuel Gas Cutting of 1045 Carbon Steel," *Journal of Material Engineering and Performance*, vol. 15, no. 6, 2006.

- [9] Olson D. L., Siewert, T. A., Liu, S., Edwards, G. R., ASM Handbook, Volume 6, Welding, Brazing, And Soldering, ASM International, 1993.
- [10] Tusek, J., Sraj, M., "Oxy-Hydrogen Flame for Cutting of Steels," *Metalurgija*, vol. 3, pp. 211-215, 2007.
- [11] K. Taniguchi, "The Hydrogen Gas Cutting System," *Komatsu Technical Report*, vol. 50, no. 154, 2004.
- [12] Osawa, N., Sawamura, J., Ikegami, Y. and Okamoto N., "Study of Heat Transfer during Piercing Process of Oxyfuel Gas Cutting," *Welding in the World*, vol. 56, pp. 2-10, 2012.
- [13] Martin-Meizoso, A., Aldazabal, J., Pedrejon, J., "Resilience and ductility of Oxy-fuel HAZ cut," *Fracture and Structural Integrity*, vol. 30, pp. 14-22, 2014.
- [14] D. Geary, *The Welders Bible*, 1980.
- [15] R. D., "Mathematical Theory of Heat Distribution During Welding and Cutting," *Welding Journal*, vol. 24, pp. 220-234, 1941.

- [16] Suitsu, K., Yasuda, T., "Some Investigation Regarding Oxygen Cutting (Report 5) -Effect of Preheat Variation on the Cutting Efficiency-," *Journal of the Japan Welding Society*, vol. 30, no. 10, pp. 733-739, 1961.
- [17] Sutsisu, K., Yasuda, T., "Somve investigations Regarding oxygen Cutting (Report 2) -Effect of Steel Temperature on the Cutting Efficiency-," *Journal of the Japan Welding Society*, vol. 29, no. 6, pp. 490-497, 1960.
- [18] M. Nakanishi, "Study of Preheating Flame on Oxygen Cutting (Report 1) - Examination of the Heating Effect on the Cut Material-," vol. 37, no. 8, pp. 839-844, 1968.
- [19] M. Nakanishi, "Study of Preheating Flame on Oxygen Cutting (Report 2) - Activation Effect on the Material Surface-," *Journal of the Japan Welding Society*, vol. 37, no. 10, pp. 1108-1114, 1968.
- [20] M. Nakanishi, "Study of Preheating Flame on Oxygen Cutting (Report 3) - Effect of Preheating Flame on material Thickness to be Cut-," *Journal of the Japan Welding Society*, vol. 37, no. 11, pp. 1260-1287, 1968.
- [21] M. Nakanishi, "Study on Gas Cutting Relating to Oxygen Pressure and Maximum Cutting Thickness," *Journal of the Japan Welding Society*, vol. 38, 1969.

- [22] I. Ueda, "Effects of the Acetylene Pressure in the Gas Cutting (Report 1)," *Journal of the Japan Welding Society*, vol. 24, no. 11, pp. 421-423, 1955.
- [23] Sato, J., Ohtani, H., Hirano, T., "Ignition Process of a Heated Iron Block in High-Pressure Oxygen Atmosphere," *Journal of Combustion and Flame*, vol. 100, no. 3, pp. 376-383, 1995.
- [24] Ivarson, A., Powell, J., Kamaku, J. Brode, G., Magnusson, C. , "The effects of oxygen purity in laser cutting mild steel; a theoretical and experimental investigation," *Lasers in Engineering*, vol. 1, p. 299, 1993.
- [25] Powel, J., Petring, D., Kumar, R., Al-Mashikhi, S., Kaplan, A., "Laser-oxygen cutting of mild steel: the thermodynamics of the oxidation reaction," *Journal of Physics D: Applied Physics*, vol. 42, p. 11, 2009.
- [26] El-Rabii, H., Kazakov, K., Muller, M. , "Experimental and theoretical study of iron and mild steel combustion in oxygen flows," *Journal Physics of Fluids*, vol. 29, 2017.
- [27] A. Wells, "Oxygen Cutting," *British Welding Journal*, vol. 8, pp. 86-92, 1961.
- [28] A. Wells, "Heat Flow in Welding," *Welding Journal*, vol. 31, pp. 263-267, 1952.

- [29] Terasaki, T., Kitamura, T., Miyamoto, Y. Fujji, T., "Heat Input Generated in Plate by Gas Cutting Process," vol. 10, pp. 197-204, 2009.
- [30] Osawa, N., Sawamura, J., Ikegami, Y. and Yamaguchi, K., "Study on the Relationship Between the Heat Transfer Characteristics of Preheating Gas and Cutting Performance of Oxyfuel Gas Cutting Performance of Oxyfuel Gas Cutting,," *Welding International*, vol. 29, no. 7, pp. 502-520, 2015.
- [31] Y. Ikegami, "Study of Oxy-fuel Cutting," *International Institute of Welding*, vol. I, no. 1322, 2017.
- [32] Bae, K., Yang, Y., Yi, M, Park, C. , "Numerical Analysis of Heat Flow in Oxy-ethylene flame cutting of steel plate," *Journal of Engineering Manufacture*, vol. 232, no. 4, pp. 742-751, 2018.
- [33] Zhou, B., Liu, Y., Tan, S. , "Efficient Simulation of Oxygen Cutting using a Composite Heat Source Model," *International Journal of Heat and Mass Transfer*, vol. 57, pp. 304-311, 2013.
- [34] Anisimova, A., Knyazeva, A., "Model of Oxygen Cutting of a Metal Plate with Chemical Heat Release," *Journal of Combustion, Explosion, and Shock Waves*, vol. 52, no. 1, pp. 53-61, 2016.

- [35] Osawa, N., Jashimoto, J., Sawamura, J. Kikuchi, J., Deguchi, Y. Yamaura, T., "Development of Heat Input Estimation Technique for Simulation of Shell Forming by Line-Heating," *Computer Modeling in Engineering & Sciences*, vol. 557, no. 1, pp. 1-11, 2008.
- [36] Tomita, Y., Osawa, N., Hashimoto, K., Shinkai, N., Sawamura, J. , Matsuoka, K., "Study on Heat Transfer Between Gas Flame and Plate during Line-heating Process," *Practical Design of Ships and Other Floating Structures*, pp. 389-396, 2001.
- [37] Matsuyama K., Moriyasu, M. and Nishiguchi, K., "Estimation of Radial Heat Flux Distribution on Plasma Arc Cutting with a Least Squares-collocation Method on the Boundary," *Transactions of the Japanese Welding Society*, vol. 22, no. 2, pp. 75-81, 1991.
- [38] H. Murakawa, Introduction to Numerical Methods in Welding Mechanics, 1985.
- [39] "Tanaka Torch & Tip," Tanaka Web Catalogue. [Online].
- [40] WES 2801, Quality Standar for Gas Cut Surface, The Japan Welding Society, 1980.

- [41] Adams, B.M., Bauman, L.E., Bohnhoff, W.J., Dalbey, K.R., Ebeida, M.S., Eddy, J.P., Eldred, M.S., Hough, P.D., Hu, K.T., Jakeman, J.D., Stephens, J.A., Swiler, L.P., Vigil, D.M., and Wildey, T.M., Dakota, A Multilevel Parallel Object-Oriented Framework for Design Optimization, Parameter Estimation, Uncertainty Quantification, and Sensitivity Analysis: Version 6.0 User's Manual, Sandia National Laboratories, 2014.
- [42] H. Schwefel, Numerical Optimization of Computer Models, Wiley-Blackwell, 1981.
- [43] "Diagram, Iron-carbon equilibrium," Encyclopedia Britannica, Inc.. [Online].

List of Publications

Journal Papers

- [1] C. Pinzon, N. Osawa, Y. Ikegami, “Influence of Preheating Flame Composition on Oxy-Hydrogen Gas Cutting Efficiency” The 29th International Ocean and Polar Engineering Conference. (2019, July 15)

Proceedings

- [1] C. Pinzon, N. Osawa, Y. Ikegami, “Study of Gas Composition on Local Heat Transfer Efficiency in Oxy-Hydrogen Gas Cutting” Conference Proceedings: Japan Society of Naval Architects and Ocean Engineers (JASNAOE)

Under Review

- [1] C. Pinzon, N. Osawa, Y. Ikegami, “Study of the Influence of the Preheating Flame Characteristics and the Oxy-fuel Gas Cutting Performance” Journal of Japan Society of Naval Architects and Ocean Engineers.

Acknowledgements

First and foremost, I would like to thank my supervisor, Naoki Osawa, for the patient guidance, encouragement, and advice he has provided during my time as his student. I appreciate all his contributions, and suggestions to make my Ph.D. experience productive and inspiring.

I would like to thank the members of my dissertation committee: Masahiko Fujikubo, Ninshu Ma, and Seiichiro Tsutsumi for generously offering their time, support, guidance and good will throughout the preparation and review of this document.

I would like to acknowledge the support from Air Water Inc., which made its R&D center available to carry out all the experimental test during this study. I would like to thank Yuichi Ikegami for their continuous support and help during the experiments.

I gratefully acknowledge the financial support from Instituto para la Formacion y Aprovechamiento de los Recursos Humanos (IFARHU), and the Technological University of Panama, for their joint support through their scholarship program that allowed me to pursue my graduate school studies. My sincere thanks also go to Adán

Vega Sáenz for offering me the opportunity to study in Japan, and for all the help and useful advice during these five years.

Lastly, I would like to thank my family for all their love, support, and encouragement. Above all, I would like to thank my wife Franchesca González, whose unconditional support throughout my Ph.D. studies is so appreciated. Thank you.

César De Jesús Pinzón Acosta
Osaka University
July 2019